Production of Automotive Aluminum Alloys AA5182 Thin Sheet Material using the Horizontal Single Belt Casting (HSBC) Process

Cheng-Hung (Jason), Hsin

Department of Mining and Materials Engineering
McGill University
Montreal, Canada

A thesis submitted to McGill University in partial fulfillment of the requirements of the degree of Master of Engineering

Abstract

In this thesis, both numerical and physical modeling studies were performed to analyze the effects of an inclined metal feeding system on the fluid flow behavior. Temperature distributions, as well as the solidification process, were also modelled. The material of interest was aluminum alloy AA5182, a type of material used quite heavily in automotive and marine applications. For the numerical model, a Computational Fluid Dynamics (CFD) simulation was built, using the commercial ANSYS Fluent software platform. The model incorporates the Volume of Fluid (VOF) method to track and locate the surface between fluids. In terms of the viscous model, the K-OMEGA SST was adopted, so as to evaluate both the near wall, and the free stream, regions of fluid flow. Flow instabilities, vortex formation, as well as the generation of small turbulent flows at the meniscus gap, were observed. In addition, temperature profiles and their associated solidification mechanisms are presented and validated against the experimental results. For physical modelling, AA5182 thin strips were produced via the pilot-scale MMPC- HSBC system. Various analyses, including microstructures, porosity distribution, SEM & BSE analysis on the secondary phases and surface quality, were conducted. Results have shown the capability of the HSBC process to produce high quality aluminum alloy strips with superior microstructures versus those produced with the Direct Chill (DC) process. Lastly, hot ductility tensile tests were carried out on some of the as-cast HSBC samples. The purpose was to determine the best rolling temperature, as an in-line hot rolling process is necessary to reduce the strips down to the desired dimensions. It was found that rolling should be applied at temperatures lower than 0.6Tm (melting point), to prevent brittle fracture.

Resume

Dans cette thèse, une modélisation numérique est réalisée pour analyser les effets d'une inclinaison du plan de remplissage du métal sur le comportement du flux et de l'écoulement de métal pendant le procédé. La distribution de la température ainsi que les modes de solidification ont également été modélisés. Tous ces facteurs jouent un rôle important dans l'obtention des bandes de qualités avec le procédé (HSBC). Le matériau en question dans cette étude est l'alliage l'aluminium AA5182. C'est un alliage très répandu dans les applications de l'industrie l'automobile et marine. Pour la partie modélisation, un model numérique basée sur la dynamique des fluides (CFD) a été développé en utilisant le logiciel ANSYS Fluent. Le modèle utilise la méthode du Volume du Fluide (VOF) pour appréhender la surface entre les fluides. Un modèle de fluide visqueux K-oméga SST a été adopté dans cette étude pour évaluer le comportement de l'écoulement du métal dans les zone porches des bords et les régions à écoulement libre. Des instabilités du flux et de l'écoulement, la formation de vortex, ainsi que les petites turbulences de l'écoulement sont générées au niveau de l'espacement du ménisque. Par ailleurs, le profil de température associé aux mécanismes de solidifications sont discutés et validés avec les résultats expérimentaux obtenus sur des essais réalisés sur la machine du MMPC (Centre de Transformation des Metaux de l'Universite McGill). Des bandes minces en aluminium AA5182 ont ainsi été produites. Des caractérisations microstructurales ont été faites sur les bandes obtenues, ainsi que observations aux microscope électroniques à balayage (SEM). Une analyse quantitative effectuée sur les microstructures a permis d'avoir une taille ainsi qu'une distribution des pores dans les pièces réalisées avec le procédé (HSBC), mais également de voir que la qualité ces derniers était acceptable. Enfin, des essais de traction à chaud sont réalisés sur certains échantillons dans le but d'avoir une idée sur la température de laminage qui est l'étape suivante à effectuer pour réduire l'épaisseur des bandes produites. Par conséquent, il a été trouvé, que la température de laminage doit être en dessous de 0.6 Tf pour éviter les fissures pendant le process.

Acknowledgments

First, I would like to thank my supervisors, Prof. Roderick I.L. Guthrie and Dr. Mihaiela Isac for their never ending supports and encouragements throughout my master's study at McGill University. Being more than just supervisors, they are also the most important mentors in my academic life. Not only have they introduced me to the fascinating field of process engineering, but have also taught me the great value of being persevering in face of challenges and the importance of being a team player. Without their enlightening guidance, I would have never imagined being able to accomplish anything fully.

I would also like to express my deepest gratitude to all the friends I have met and worked pleasantly with at McGill University, as well as at McGill Metals Processing Center (MMPC), as well as at MeSim Inc. It has been of great pleasure to be able to work with Dr. Luis E. Calzado, Dr. Mianguang Xu, Dr. Samuel Rodrigues, Dr. Ameth Maloum Fall, Mr. Usman Niaz, Mr. Giacomo Di Silvestro and Mr. Justin Lee. In addition, my thanks also go to the CO-OP students, Xiuyuan (Shawn) Zhu, Karim Selim and Ajay Panicker. Without them, it would have not have been possible to come this far and to present the works we had together accomplished. I am also grateful for Natural Sciences and Engineering Research Council of Canada (NSERC), and the industrial supporters of the MMPC, for their generous financial support that made my research and stay at McGill so enjoyable.

Most of all, I want to give my most sincere thanks to my parents. Your unconditional love, support and encouragement throughout these seven years has been the driving force for me to press onward, and to strive to be better. I would like to dedicate this dissertation to you. Thank you.

List of Figures

List of Tables

Table of Content

Introduction

In response to the global demand for greener energy and environment, transportation industries have been searching ways to either increase the usage of light metals materials, or to “lightweight” steel itself, in order to reduce the fuel consumption and emission of harmful gases. It is with no doubt that by reducing the weight of cars, societies as well as the whole ecosystem can benefit. Typical metal sheet production methods such as Conventional Continuous Casting (CCC) process or Direct Chill (DC) casting process can be extremely expensive. For that, the goal to transition to higher percent usage of aluminium alloys has remained quite challenging in the industries. Thankfully, substantial amount of research has been devoted lately to develop strip casting technology, with the hope to reduce the total operational cost whilst being able to maintain the products’ quality for their applications. Horizontal Single Belt Casting (HSBC) is a Near Net Shape casting method capable of producing alloy strips directly from their molten form. The working principle of HSBC relies on pouring superheated molten alloy through specially designed nozzles onto a single, continuously water-cooled, horizontal moving belt. The purpose is to achieve friction free, iso-kinetic feeding mechanism, meaning having the melts coming with a speed matching the one of the moving belt. This will allow the strips to freeze under quasi-static, near zero-turbulence conditions to ensure the final quality [1]. Numerous studies toward the design of delivery system have been carried out to fulfill this crucial aspect of HSBC process. Different nozzle configurations, such as the one that has the melt free falling from a slot nozzle, or the design that has it impinging first onto an inclined plate, have been modeled using numerical simulations to study their performances [2]. The latter were found to be more efficient, as the inclined plate allows the fluid flow to be reorganized by both frictional and gravitational forces. Some important mass and heat transport phenomena can also be very well predicted with these models. All these will be discussed later in more details. In terms of the material studied, aluminum alloy AA5182 was selected for it is one of the primary materials used for structural applications in the automotive and marine industries. It has a freezing range of approximately 61°K. Given this freezing range is much smaller in comparison with most other 5000 series aluminum alloys (such as AA5754), the strip casting process is currently more feasible for AA5182 since rapid solidification is one of the important requirements for the process to succeed. [3] Finally, for the first time, the hot ductility tensile tests were performed in order to estimate the suitable rolling temperature of the as-cast strips coming straight from the delivery system. In-line hot rolling was attempted, and the strips had experienced brittle fracture. Hence it was of interest to determine the temperature range of rolling to avoid formation of cracks. In this thesis, findings from numerical simulations, together with the experimental results are presented.

1. Chapter 1 Literature Review

1.0 Introduction

With exponentially growing demands for high strength, light weight structural materials such as aluminum alloys, process engineers have faced great challenges in providing solutions to improve and cut down the cost of the already existing processing methods. With decades of research, strip casting technology have gradually emerged and differentiated themselves from the current conventional production methods, for their capability to produce strips with superior quality and with less spending. Strip casting is a Near-Net-Shape Casting (NNSC) processing technique. It means the raw products that come out of the initial casting stage prior to the rolling have already possessed the dimensions close to its designated final shape. This NNSC technology shows great potential as it offers an economic and efficient approach without having to compromise the quality of the final products. In this literature review, three specific types of strip casting technology 1) Twin-Roll Casting (TRC), 2) Twin Belt Casting (TBC), and finally 3) Horizontal Single Belt Casting (HSBC), have been discussed. Following is a brief section introducing aluminum alloys used in automotive industries. Lastly, a section of the review is dedicated to the principles of Computational Fluid Dynamics (CFD), showing how CFD can be used to help simulate metallurgical processes. Details on specific types of solution schemes are reviewed.

1.1 Technical Development in Near Net Shape Strip Casting of Aluminum Alloy Sheet Materials

1.1.1 The Twin Roll Casting Process

Twin Roll Casting (TRC) process has come a long way since the mid 1800's. It was first conceived by an English inventor, Sir Henry Bessemer in 1865. Ever since, substantial amount of research focusing on refining the TRC process have been carried out continuously up to the modern times.

It was first designed to directly produce steel strips from the molten iron. Lately, around the 1950's, the first ever commercialized TRC technology was also applied to the production of non-ferrous light metals, such as aluminum alloys[1]. Aluminum alloys, having nearly half of the weight of steel and a better strength to density ratio, have gained a lot of interest from the automotive industry. Rather than using the conventional Direct Chill (DC) process that requires higher demand of energy and cost, TRC has proved itself to be a better option for the aluminum industries. Other than the economic perspective, TRC has also been shown to have much superior characteristics that make this technology one of the most popular strip casting techniques. In general, it consumes far less energy, and provides possibilities for diversification in terms of design. It is also able to produce materials with better microstructure and distribution of intermetallic particles. Due to its efficient cooling capability, increased solid solubility can be achieved as to offer a much better overall mechanical strength.

1.1.1.1 Principles and Machine Layout of TRC

The process of Twin Roll Casting (TRC) involves feeding molten metals into two counter-rotating, robust rolls. These rolls exert the required forces on the solidifying melts for deformation, while simultaneously providing the necessary cooling for solidification. The as-cast strip will then be hot-rolled subsequently into the desired shape.

What makes TRC stands out are due to its following unique characteristics (2).

1) A high heat flux at the roll-liquid metal contacting interface promotes a much uniform and higher rate of solidification.
2) TRC allows friction free casting, meaning it's able to achieve the same velocity between the tangential speed of the rolls and the solidified metals strips.

3) One single operation that integrates both casting and rolling. As the strip comes out of the first stage of casting has already the shape close to its final form, the process can eliminate extra steps of re-heating and hot rolling process.

TRC can come into several forms, that is, the rolls can be arranged in either horizontal, or vertical fashion, as shown in the schematic diagram below.

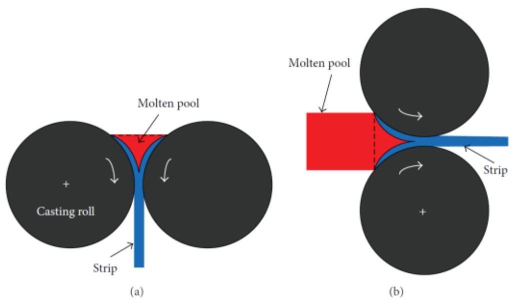

Figure 1.1 a) Vertical twin roll strip caster b) Horizontal twin roll caster

In general, the TRC caster can be divided into two major categories 1) horizontal Twin Roll Strip Caster (HTRSC) and 2) Vertical Twin Roll Strip Caster (VTRSC). The table below provides a brief comparison between the two setups.

Table 1-1 Comparison of the horizontal twin roll strip caster and the vertical twin roll strip caster

Type	Horizontal twin-roll strip caster	Vertical twin-roll strip caster
Lubricant	Use	No-use
Casting speed	1–15 m/min	30–150 m/min
Roll force	>1 KN/mm (width)	<0.5 KN/mm (width)
Strip thickness	4–7 mm	2–4 mm
Cooling rate	Low	High

In the early stage of commercialized TRC operations for aluminum alloys, conventional TRC's rolls setup is normally in the horizontal orientation. The surface of the two rolled were lubricated with a water-base graphite suspension to prevent melts to stick on the interface. While the melt is passing through the counter-rotating rolls, the heat of the molten alloy is extracted to the rolls due to the high temperature gradient. As mentioned, TRC has a very efficient cooling mechanism, and the major contributor to this characteristic is due to the continual deformation of the solidified structure and the thermal conductivity of the rolls' material. The rolls can exert desired amount of load (separating force) that is greater than the stress flow of the solidified alloy, hence promote plastic deformation. These deformations allow better contact between the rolls and the alloys. The rolling force can be calculated as follows[2].

$$F = 1.55\sigma_{yield} W \left[1 + \sqrt{\frac{R(h_2 - h_1)}{4(h_1 - h_{mean}/2)}}\right] \sqrt{R(h_2 - h_1)} \tag{1}$$

where

$$H_{mean} = \left[h_1 - \frac{h_2 - h_1}{2}\right] \tag{2}$$

Here σ_{yield} is the mean yield stress of the specific alloy. W is the width of the strip; R is the outer radius of the rolls. h_1 is the thickness of the strip right at the point where complete solidification occurs, and h_2 is the thickness of the strip at the point of exit. H_{mean} is the mean thickness of the strip. From the equation, it is clearly seen that the amount of applied force greatly depends on the yield stress of the materials. It is expected that with alloys having much higher alloying additions, the rolling force should be increased due to increased yield stress.

As for the thermal conductivity, the rolls in the early conventional TRC's were made of steel as it has a fairly large thermal conductivity. Rapid cooling is achievable as it enhances heat transfer from the melt to the rolls. Nevertheless, as mentioned, the extra layer of lubricant applied on the surface can reduce the heat flux i.e. has a negative effect on cooling efficiency. Although this original TRC process already possesses great cooling, the casting speed, as well the system alloys suitable for casting process, were hence limited. Some research has been devoted to optimize the cooling mechanism by investigating the selection of new roll materials to avoid the need for lubrication [3-5].

Haga et al. [5, 6] investigated the conventional TRC for aluminum alloys (CTRCA) and showed that by replacing the roll's material from steel to copper, lubrication can be eliminated, and additionally, it improves the cooling efficiency. With this finding, the research team constructed a novel modified TRC process called Hydrostatic Press Twin-Roll Caster (HPTRC) (Figure 1.2).

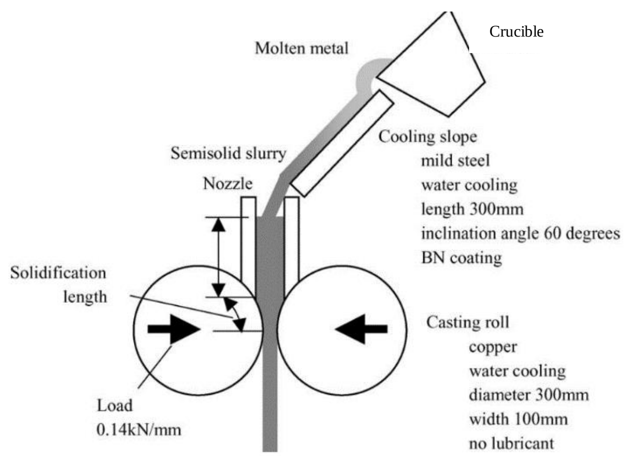

Figure 1.2 Schematic illustration of HPTRC

Different from the CTRCA, HPTRC is a vertical twin roll casting process with a nozzle mounted right on the rolls, as shown below. In this setup, the melt can be perfectly directed along the processing line without having to worry about the leakage from the clearance between rolls and nozzle, as in the case of CTRCA. Moreover, the nozzle can be moved accordingly to cast the strip to the desired thickness. It is known that the contact length, as indicated in the schematic diagram, has a profound influence on the thickness of strips produced. By properly adjusting the nozzle position, the control over the casting thickness can be better managed [5].

One thing worth noticing is that oscillation of the meniscus can occur at the tip of the nozzle during casting. This oscillation has a negative effect, as it leaves periodic marks on the surface of strips. This issue can be detrimental when the roll speed is higher than 20m/min. Nevertheless, the surface instability problem can be solved with high hydrostatic pressure by increasing the melt head contained in the nozzle. With higher melt head, the oscillation can be stabilized.

As mentioned, the other major change is the use of copper rolls. Copper rolls, which have a higher thermal conductivity than steel, are implemented and tested. The results show a much more rapid heat transfer performance; hence rapid solidification can be achieved. Due to this improvement, lubricant is no longer necessary. In the CTRCA, lubricant is used to prevent sticking. It is especially severe when the temperature of the roll surfaces is too high. This usually occurs in materials with low thermal conductivity. In HPTRC, the issue of sticking is solved as the copper rolls provides higher cooling rate and thermal conductivity. The materials would solidify before they have a chance to stick to the rolls [7].

With all these modifications, the casting speed, which is directly related to the total mass of production, can be greatly improved.

1.1.2 The Twin Belt Casting Process

Another continuous strip casting process that is popular for aluminum sheet manufacturing industries is the Twin Belt Casting (TBC). The process was first conceived by Clarence W. Hazelett in 1919 [8]. He is considered as one of the pioneers of continuous casting technology. Having experience working with various casting processes such as single and twin rolls casting, he found that mold surfaces that are movable and parallel can be a very good casting mechanism to produce high quality light metal thin slabs for strip production. The first ever commercialized TBC caster was launched in the 1960's. Continuous research and improvement have been carried out by three generations of the Hazelett family. Nowadays, TBC technology has been successfully adopted and accounts for nearly 30% of the world's continuous casting output of rolled aluminum alloys. [9] Different from the sheet products produced from Twin Roll Casting (TRC), which are mainly applied for small and narrow components due to the extremely high cooling solidification, the sheet products from TBC have much better formability. In TRC, with its very high cooling conditions, the metallic sheets possess finer intermetallic compounds and recrystallized grains. Needless to say, compared to traditional Direct Chill (CD) casting, both TRC and TBC offer better control over the solidification process and therefore, they are capable of making strips of uniform quality and with very little defects such as segregation, and inverse segregation. Both processes are simpler than the DC casting process, which requires extra steps of multiple cutting and hot rolling [10]. In terms of the advantage of the TBC over the TRC process, TBC is less restricted with the type of alloys. Figure 1.3 shows a quick schematic comparison of a DC and TBC process line.

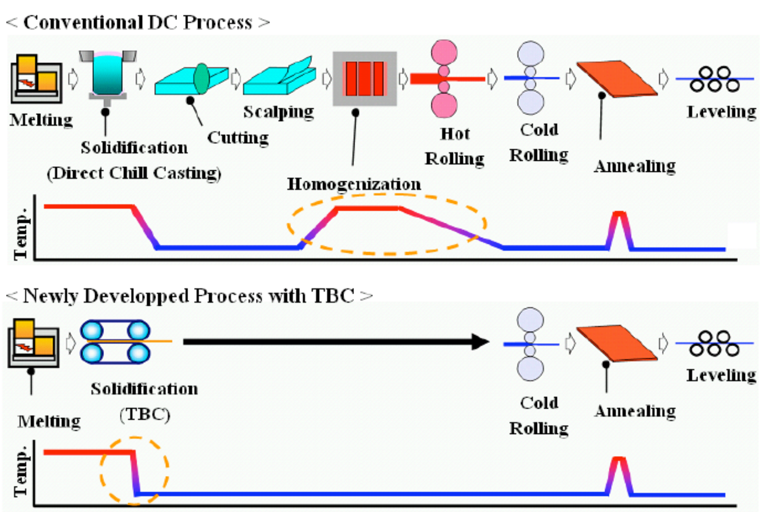

Figure 1.3 The production processes of Aluminum alloy sheet for TBC and DC

1.1.2.1 Principles and Machine Layout for TBC

As shown in Figure 1.4 below, the major component of the Twin Belt Caster is the mold region, in which the liquid metal is confined by one upper belt and one lower belt, both made of low carbon steel with 1.2mm thickness. The belts are normally coated with metallic/ceramic mixture, so as to provide necessary surface parting and heat transfer phenomena.

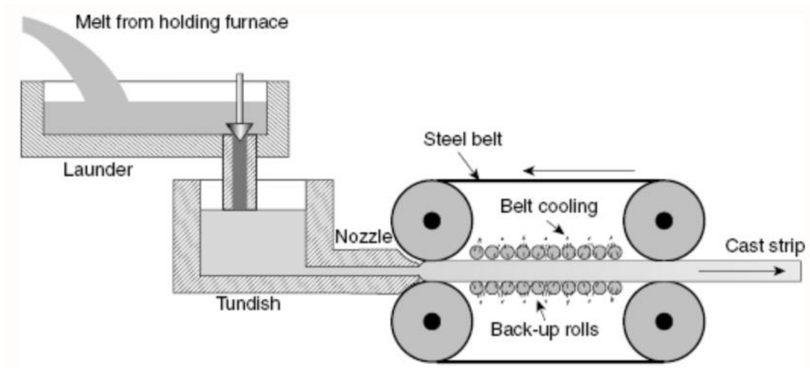

Figure 1.4 Schematic of TBC

As can be seen, the steel belts are wrapped around multiple grooved pulleys. Before the molten metal enters the belt region, pre-heaters mounted on the upstream pulleys will start heating the belt so as to pre-expand it, in order to avoid thermal distortion during casting. The pulleys, located downstream, are responsible for applying tension and driving the belts, so as to obtain the required flatness. In general, the thickness of the cast strip is determined by carriage spacers, that can be varied between 12mm, all the way to 75mm.

During casting, one of the crucial components of the TBC is the belt cooling system. The heat extraction is attained with fast film water cooling located on the back side of the rotating belts. Typically, the upper surface temperature of the belt can be maintained at temperature below 110^{o}C during the contact with molten metal, and around 80^{o}C on the side of the water film. With the orientation of the grooved back-up rolls, the cooling water can have full coverage to ensure constant cooling efficiency.

In terms of the metal feeding, during the casting operation, metal melt is injected into the mold cavity through a nozzle connected to a tundish, as shown in Figure 1.5. Inert gas shrouding is applied to the small gap between the belt and the nozzle so as to minimize the oxygen content and also, to control heat transfer rates between the solidifying metal and belt interface.

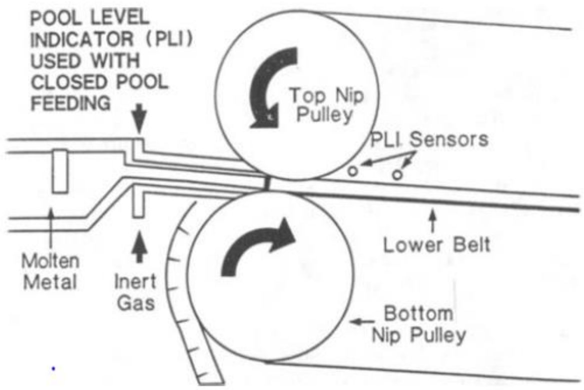

Figure 1.5 Metal delivery system

After casting, the as-cast strip will undergo an in-line hot rolling process to have its thickness reduced up to 70%. Normally, there can be 1, 2, or 3 rolling mill stands in the whole setup. Compared to the DC technique, the amount of post-treatments in the TBC are significantly fewer, and more efficient. This physically translates to lower capital and operation costs [8, 11-13].

The first ever successful Hazelett caster was installed by Alcan in 1959. Ever since, the caster has been producing good quality aluminum alloy coil from 1xxx, 3xxx, and 8xxx series in 1971. Recently, more and more other series of aluminum alloys has become of interest, such as the 5xxx and 6xxx that are in high demand by the automotive industries [9].

1.1.3 Single Belt Casting Process- Horizontal Single Belt Casting (HSBC) & Direct Strip Casting (DSC)

Single Belt Casting is the most recently developed near net shape continuous strip casting process. The strip casting process was conceived independently by Drs. J. Herberston and R. Guthrie, in Canada, as the HSBC, and by W. Reichelt, K. Schwerdtfeger, P V. Spikler and E. Feuerstacke, in Germany, as the Direct Strip Casting (DSC) process. Both patents were filed in 1988. The DSC process began its development in 1986 at SMS Siemag AG and the Technical University of Clausthal [14]. In parallel, the HSBC process began in 1986, in Australia, then continued its development at the McGill Metals Processing Centre, ten years later. The concept of both processes is similar to that of the Pilkington float glass manufacturing technology, where the molten glass is poured continuously onto the molten tin bath and is allowed to slowly move and solidify to glass strip. The HSBC belt casting process has been applied to produce both steel and light metal sheets, such as aluminum alloys for the automotive and aerospace industries. This novel continuous strip casting technique, however, is still going through a substantial amount of research in order to be fully developed. Unlike TRC and TBC, which both have gone through more than 100 years of developments, single belt casting process has not yet been fully commercialized. The first pilot-scale HSBC caster was built by Hazelett at the request of BHP and its inventors in the 1989. It has gone through several changes and improvements ever since, in terms of delivery systems, pre-heating and melting units, as well as automation control. In the meantime, the Direct Strip Casting (DSC) began its first casting trials in the 1989 and reached commercialization in 2012.

1.1.3.1 Principles and Machining Layout

Single belt casting is considered as the latest and most simplified form of the TBC alternatives. Compared to both TRC and TBC, the single belt casting process is much easier to operate. Given the significant reduction in terms of the size of process lines, the capital investments, as well as the operating costs, overall expenses can be reduced tremendously. Currently, one of the pilot-scale HSBC casters is now operating at the High Temperature Melting, Casting, and Simulation laboratory, of MetSim Inc., in Montreal, under the supervision of Drs. Mihaiela Isac and Roderick Guthrie. Numerous research efforts have been poured in to further commercialize and refine the HSBC process. Different from the TBC, the HSBC has one single moving water-cooled belt. Figure 1.6 shows a schematic diagram and a real machine of an HSBC pilot-scale caster.

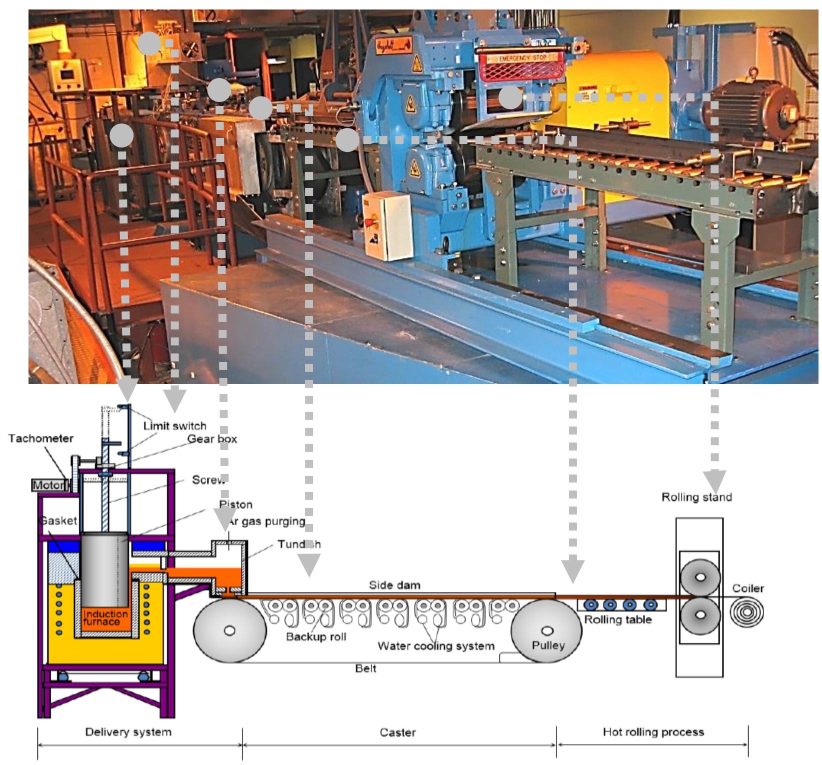

Figure 1.6 Schematic and photo of the pilot scale HSBC caster

Prior to casting, the aluminum alloy is prepared and melted in the induction furnace. The melt is superheated and transferred to the casting station right underneath the displacement piston. The piston, as well as the whole delivery system, are preheated to a temperature slightly higher than the liquidus temperature of the alloy. Once ready, the piston will start pushing downwards, so as to displace the alloy melt upward to fill the delivery launder. The downward speed of the piston is pre-calculated, in order to coordinate with the speed of the moving belt, so as to create an iso-kinetic feeding mechanism to produce the strip of the desired thickness and to enhance the surface quality. The metal delivery system (launder) is made up of three different parts, that are: 1) an entry chamber, 2) a head control chamber, and 3) an output chamber. Within the launder, a couple of little dams are implemented before the head control chamber in order to minimize the turbulent flow. As for the moving belt, which is made of steel, it is coated with graphite layer to ensure a smoother bottom surface of the cast strip. The high rate of solidification in the HSBC process is achieved by constantly running low temperature water underneath the belt to ensure sufficient heat extraction from the melt to the moving belt. Learning from past experiences in the TBC development, the belt in the HSBC process is "cold framed" so as to tension the belt area first being contacted by molten metal. That, together with multiple magnetic backup rolls acts to prevent belt distortion and thermal expansion during casting. During casting, the melt is allowed to flow through a nozzle on to the cooling belt where most of the solidification is expected to occur. The semi-solid alloy is then passed on to the run-out cooling table, and into a pinch roll/mini-mill station. The pinch roll station can further reduce the thickness of as-cast strip by ~20% [15, 16].

In the TU Clausthal's Direct Strip Casting (DSC), the machine layout is very similar to that of HSBC, and the overall set-up is shown in Figure 1.7.

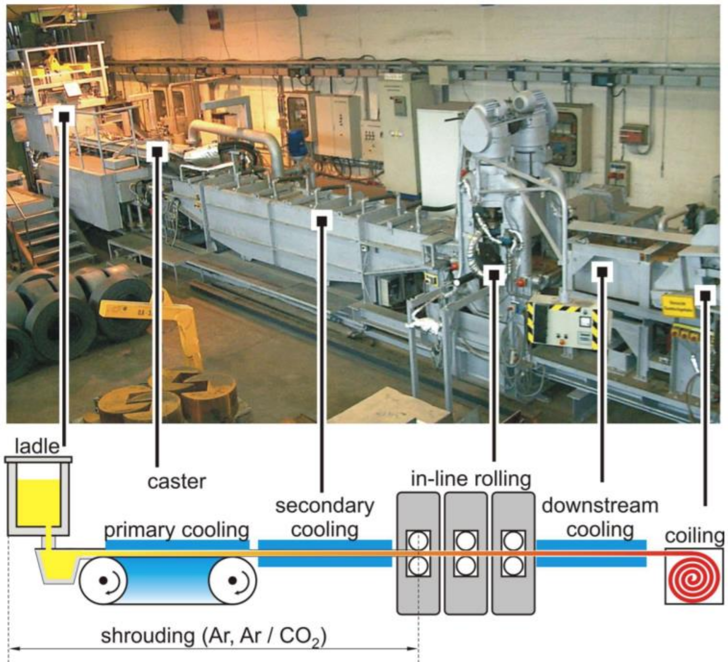

Figure 1.7 Schematic and photo of DSC process caster

Similar to the HSBC process, the ferrous alloy melt is delivered through a dispenser system onto a single revolving steel conveyor belt. The belt acts as the mold that is consistently water-cooled from below. In order to prevent belt distortion, suction is applied to the belt by maintaining the pressure under it at 0.7 atm [15]. Different from the HSBC, the DSC has its primary and secondary cooling region completely protected in an Ar, Ar/CO_2 atmosphere, so as to prevent the loss of ferrous material through oxidation, as this could have an adverse effect on the strip quality, both on a microstructural level and at its surface. In the primary cooling region, the strip is readily solidified and is able to achieve a thickness around 20mm[15]. The strip then enters the secondary cooling region, also known as the homogenization zone for further temperature adjustment. In this region, the solidified strip will be subjected to homogenous temperature distribution that is suitable for in-line rolling. The temperature can be adjusted higher or lower depending on the strip's condition. Typically, the yielded strip from the secondary cooling has a thickness ranging from

10~15 mm, and will then be further reduced through 3 to 4 steps of rolling, in order to achieve the desired mechanical properties and final thickness needed for coiling [17].

In the single belt casting process, it is important to ensure the melt is uniformly distributed on the belt during casting for quality purposes. This can be hard to achieve. In the TU Clausthal DSC caster, to overcome this technical difficulty, argon gas sprays are blown in the opposite direction to the melt flowing onto the belt. Additionally, an Electromagnetic Flow Synchronization System (EFSS), which is a linear inductor capable of generating a strong magnetic field, is implemented and installed close to the top surface of the melt to further enhance the melt flow profile and prevent the solidification process from being disturbed [17].

As for the MMPC-HSBC process, research has been focused on the design of delivery system's exiting nozzle to form thinner strips of 5mm. Several types of nozzles have been conceived and modeled, in order to evaluate their performance on strip uniformity, surface stability and achievable highest casting speed. Figure 1.8 shows some of the designs researched.

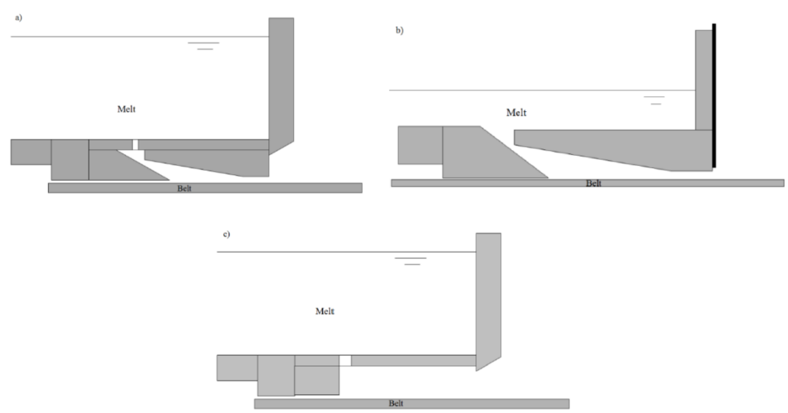

Figure 1.8 Various nozzle configurations studied

The approach taken for the HSBC system is to utilize the gravity force so as to achieve iso-kinetic flow. It is important to minimize the relative velocity between the moving belt and the alloy's melt in order to make sure of even melt distribution and stability. The quality of nozzle's surface (roughness), and the control of falling mechanism of the melt, are important conditions for obtaining good quality strips.

1.1.3.2 Previous findings

A single impingement nozzle configuration has been studied quite extensively by researchers at the McGill Metals Processing Centre (MMPC). Below, Figure 1.9 shows the schematic diagram of the delivery system used for the pilot scale MMPC HSBC caster.

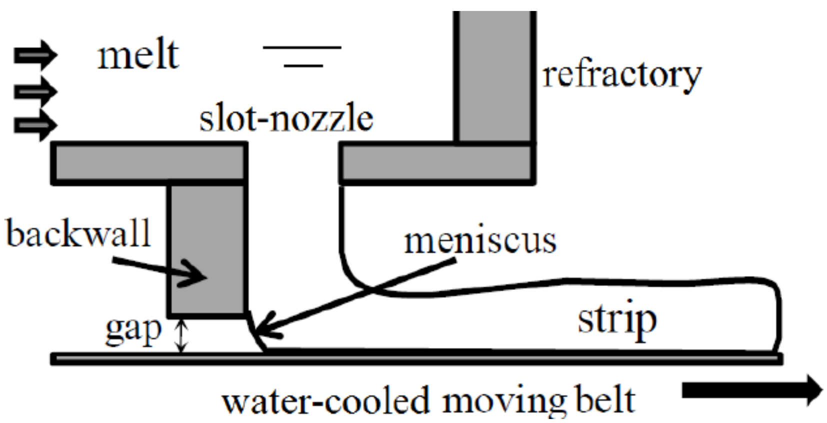

Figure 1.9 Schematic of Single impingement delivery system configuration

The Special alloy, Al-Mg-Sc-Zr strips of 70 ~ 100 mm width and 5 ~ 7 mm thickness, were successfully produced with this specific nozzle configuration at MMPC. The microstructure, as well as the surfaces of the as-cast HSBC products, had shown superior characteristics over the equivalent products cast with the Direct Chill (DC) casting process, not to mention the other conventional continuous casting (CCC) processes that are far less efficient in terms of cooling. These successes later become the foundation for another round of successes to produce larger width strips i.e. 200 ~ 250 mm, as will be presented in a later section of this thesis. In addition, due to its superior cooling mechanism and one-way cooling strategy, the HSBC process has made the production of many different aluminum alloys series now possible [18].

1.2 Aluminum Alloys Strips for Automotive Industry

Aluminum alloys, being one of the lightest non-ferrous engineering materials, has gained much attention and interest from the automotive industries. With their good strength to density ratio and excellent corrosion resistance, they are seen as a good potential substitution for steel. If successful, the body weight of an automobile can be reduced drastically with significant reduction in fuel consumption. In order to achieve all the necessary requirements for mechanical properties, it is important to have a thorough understanding of the metallurgical effects. The sheet materials for car's structural parts and body-in-white applications require an optimal combination of strength and formability. One of the most commonly seen alloy systems that is used for this specific application is the non-heat treatable Al-Mg. This system has been well studied and developed to meet the design requirement, capable of achieving an optimal balance between strength and formability [19]. This good combination is made possible due to the solid solution hardening mechanism that cause high strain within the lattice. Aluminum alloys, having a solidification temperature range below 660ºC, exhibit a FCC crystal structure. Different from iron and steel, aluminum does not go through allotropic transformations, and therefore, the achievable structural refinement during casting is very limited [20]. Thermo-mechanical post processing, such as hot rolling and age hardening play a crucial role in determining the final property of these alloys. Table 2 shows a list of the main sheet aluminum alloys that are currently used in automotive applications, together with their mechanical properties in their annealed condition.

Table 1-2 5xxx & 6xxx series aluminum alloys for automotive application- composition and mechanical properties in annealed condition

Al-Mg (AA5XXX)	Alloy designations	Yield strength (MPa)	Ultimate tensile strength (MPa)	Elongation	Strain hardening coeff. / strain ratio
AlMg3Mn	AA5454	230	110	26	0.30/0.68
AlMg5Mn	AA5182	270	130	30	0.31/0.75

AlMg5Cu	KS5030	290	140	30	0.30/0.65

1.2.1 Non Heat Treatable Al-Mg Alloys (5XXX)

For the Al-Mg system, the existence of Mg plays a crucial role in providing the high strength and good formability property for this series of aluminum alloys. Both aluminum and magnesium have the same coordination number of 12, that is, the number of atoms an element can hold around its nearest neighbors. Additionally, both have relatively similar radii, with aluminum being 0.14nm, and magnesium being 0.16nm. Due to these similarities, magnesium atoms can easily substitute in the atomic arrangement as shown in Figure 1.10, within the aluminum matrix [21].

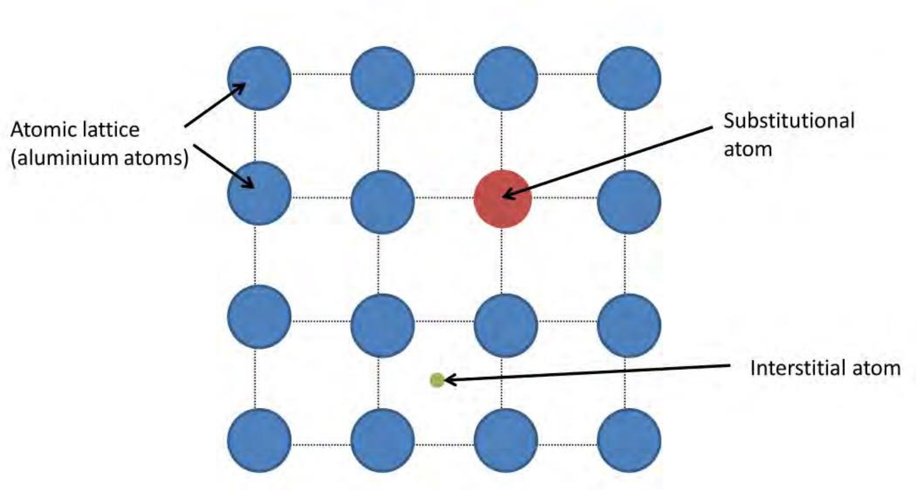

Figure 1.10 Substitutional atoms in aluminum crystal lattice

This phenomenon is a type of solid solution hardening that can strengthen the material to achieve good yield strength and meanwhile, a well-balanced strain hardening exponent (or strain hardening index) [22]. This exponent gives an indication of how elastic and easily formable a material is. For materials going through forming operations, the higher the Mg content within the alloys, the higher the value of the strain hardening exponent, as can be seen in Figure 1.11a. Additionally, there is less drop with strain at higher Mg volume fraction, as shown in Figure 1.11b.

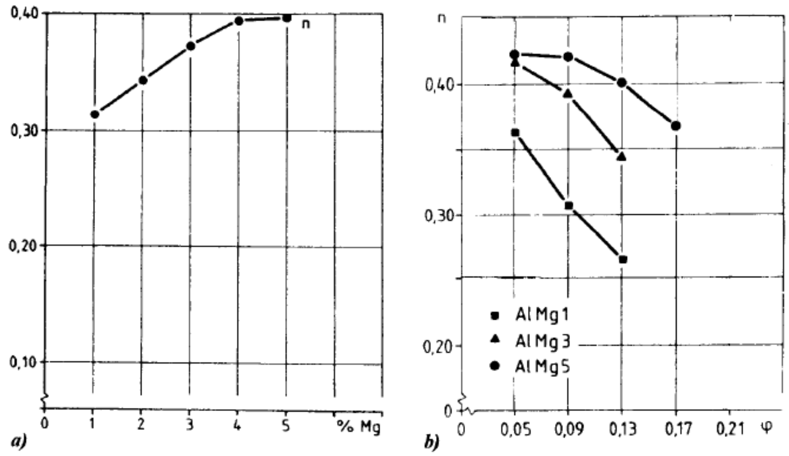

Figure 1.11 Strain hardening exponent n and its dependence on Mg content and strain

1.2.2 Aluminum Alloy AA5182

AA5182 especially is used in various applications due to its good combination of strength and formability, good corrosion resistance and weldability. It is commonly manufactured into automotive components such as liftgate inner panels, weldable and structural reinforced parts. In addition, it is also applied quite significantly in the canning industries and in marine structural applications.

According to the literature[23], the major phases that AA5182 is composed of is the α-Al (Aluminum dendrites), the iron-bearing eutectic particles Al_m (Fe, Mn) and Al_3(Fe, Mn), and finally the Mg_2Si. The phase transformations usually take place in between the liquidus temperature and solidus temperatures, that is 638°C and 577°C respectively. During solidification, the first phase to nucleate and grow consists of equiaxed dendrites of α-Al. That is followed by the main eutectic reaction, which is from liquid to the formation of iron bearing Al_m(FeMn). Along with that is some concurrent precipitation of Al_3(FeMn). As the temperature continues to drop to around 557°C, the Mg_2Si will start to precipitate at the grain boundaries [24]. Depending on the local cooling rate, the amounts of Al_m or Al_3 may vary. In this alloy, the major strength comes from the Mg_2Si solid solution strengthening, due to the size and modulus misfit. Also, at higher cooling rates, the Al_m tends to dominate over the Al_3 intermetallic. As for the effect of Mn addition, it is there to compensate for the negative effect of the Al_3(FeMn) for this particle has a needle like structure, making it very brittle. The addition of Mn can transform this into Al_m(FeMn) that is much more refined. However, it must be limited to low levels, so as to prevent the structure becoming extremely coarse again [25].

1.2.3 Processing Route for Aluminum Alloys AA5182 Sheets

Traditionally, aluminum alloys sheets for automotive application have been produced via DC-ingot casting, followed by hot and cold rolling, and finally with an annealing treatment. Nevertheless, this process can be extremely long, and expensive. For these two reasons alone, the goal of increasing the usage of aluminum alloys has remained challenging. Despite this, thanks to the invention of near net shape strip casting process, such as TRC, TBC, and HSBC, this dream has been made possible. Recently, increasingly successful results in producing aluminum alloys sheet via TRC have been obtained and even commercialized. Up until this point, almost 25% of U.S. sheet and foil volume are produced by either these roll or slab casters [9].

1.3 Application of Computational Fluid Dynamics (CFD) in Process Metallurgy

Operations in process metallurgy such as continuous casting and strip casting processes involve complex transport phenomena. These phenomena include the fluid flow behavior of liquid melts, as well as the heat and mass transfer for melt mixing, and solidification mechanism. All these factors play crucial roles in determining the efficiency of the casting process and more importantly, the quality of the casting products. Due to the nature of the process, which in the majority of the cases are multiphase problems, it requires an enormous amount of mathematical computations to provide detailed information necessary to understand the kinetics and physics behind it. Analytical solutions of most actual processes are problematic, as they require solving a series of governing partial differential equations simultaneously. Thanks to the invention of numerical methods, CFD has become a great tool to effectively solve and predict almost any given process. These results can be of great help in designing improvements, as well as to develop new processes.

1.3.1 Mathematical Description

Same as any other transport phenomena that are solved analytically, numerical solutions of fluid flow, heat and mass transfer and other related phenomenon such as turbulent behavior are governed by the fundamental conservation principles. One of the major laws that should be respected is the conservation of mass within a given control volume. In the case of process metallurgy, it is assumed that there is no energy to mass conversion, i.e. no mass is generated or destroyed. In addition, most fluids can be assumed to be Newtonian, and incompressible. Hence the continuity equation can be much simplified to the following, using index notation;

$$D_t\rho = \partial_i \mathrm{V_i} = 0 \tag{3}$$

In terms of the conservation of other properties such as momentum and energy, the equations are shown as follows, respectively;

Momentum: $$\partial_t(\rho v_j) + \partial_j(\rho v_j v_i) = \rho F_i - \partial_i P + \partial_j \tau_{ji} \tag{4}$$

Energy: $$\partial_t(\rho e_t) + \partial_i(\rho_i v_i e_t) = -\partial_i q_i + \partial_i(T_{ij} v_j) + \rho v_i F_i \tag{5}$$

It is clearly seen that all relevant governing differential equations obey the same conservation principles. With this in mind, all equations can be generalized as follows, with $\emptyset$ denoting any of the variables desired [26, 27].

$$\partial_t(\rho\, \emptyset) + \partial_i(\rho v_i\, \emptyset) = \partial_i(\Gamma\, \emptyset) + S \tag{6}$$

Here Γ is the diffusion coefficient and S is the source term, whereas $\emptyset$ can be any of the variable quantities, such as V, U, W, C, T, etc. (velocity components, conservation of species, energy). Additionally, the four terms shown in Eq.4 represent four phenomena, that is, the unsteady term, the convection term, the diffusion term, and the source term. Note that the dependent variable $\emptyset$ is always a function of space and time as shown in Eq.7.

$$\emptyset = \emptyset(\boldsymbol{x}, \boldsymbol{y}, \boldsymbol{z}, \boldsymbol{t}) \tag{7}$$

1.3.2 Discretization Equations

Given the nature of numerical solutions to partial differential equations, it always consists of sets of numbers that describe the distribution of any dependent variable $\emptyset$ in a constructed calculation domain. In order to ease the calculation, the concept of discretization was introduced. This method was later classed as discretization methods. Instead of keeping all governing partial differential equations (PDEs) as is, they are now expressed and evaluated by turning them into the form of algebraic equations. Take an arbitrary dependent variable $\emptyset$, varying in only the x direction for example, the algebraic equation can be written as shown [28].

$$\emptyset = a_o + a_1 x + a_2 x^2 \pm \cdots a_m x^m \tag{8}$$

These equations will be referred as discretization equations after this point. In order to derive the discretization equations for given differential equations, one of the most commonly used methods is the Control Volume Formulation. This method provides a much more direct physical interpretation compared to other methods such as finite difference or finite element approaches that use a Taylor series expansion. In the control volume formulation, the calculation domain is divided into a series of control volumes, with each volume surrounding one grid point. The governing differential equations are then integrated over each control volume. This gives rise to a set of discretization equations, which can be solved to predict the distribution of the dependent variable $\emptyset$ within the domain of interest.

Take a one-dimensional steady state heat conduction problem as an illustration, the governing equation is as follows;

$$\partial_i(k\partial_i T) + S = 0 \tag{9}$$

k is the thermal conductivity, T is the temperature, S is the source term, and ∂_i is the partial differentiator wrt. to distance in the x direction.

Figure 1.12 is a schematic of the grid-point cluster for a 1D simulation domain.

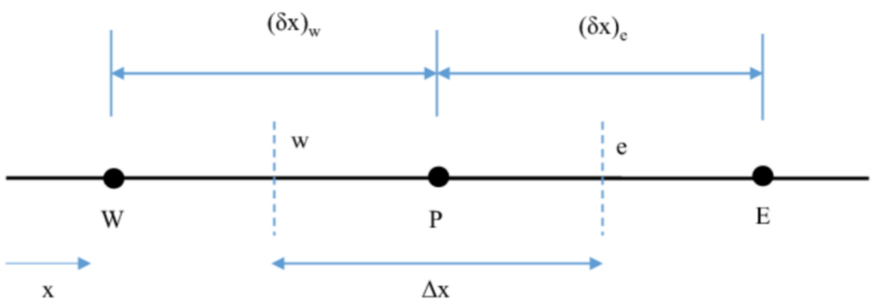

Figure 1.12 Schematic of the grid-point cluster

The point P is the point of interest with capitalized W and E being the two neighboring grid points. (W here denotes the west, and E is the east) The distance between the point is given an arbitrary length of δx. The smaller case w and e represent the interfaces that enclose each grid point to generate each control volume with length, Δx. By integrating Eq. 9 over the all control volumes, i.e. from west to east, the result obtained is

$$\left(k\frac{dT}{dx}\right)_e - \left(k\frac{dT}{dx}\right)_w + \int_w^e S\,dx = 0 \tag{10}$$

In order to evaluate the term $\frac{dT}{dx}$, a piecewise linear profile assumption is made. This assumption is much more accurate compared to stepwise linear profile that assumes the T value maintains the same throughout its surrounding control volume. Both profiles are sketched in Figure 1.13 below to give better physical understanding.

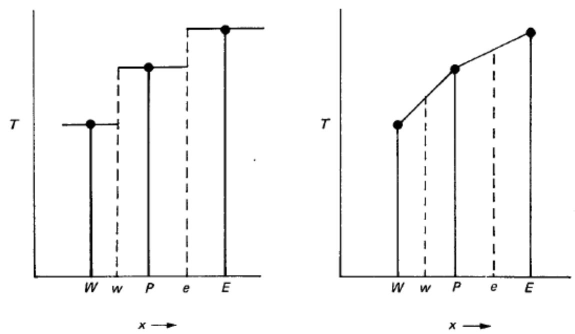

Figure 1.13 left: stepwise profile   right: piecewise profile

With the application of the piecewise profile assumption, the resulting derivative of eq.10 can be re-written as

$$k\frac{(T_E - T_P)}{(\delta_x)_e} - \frac{k(T_P - T_W)}{(\delta_x)_w} + \bar{S}\Delta x \tag{11}$$

with $\bar{S}$ being the average value over the control volume. This discretization equation can be further simplified, by replacing a couple of the terms:

$$a_P T_P = a_E T_E + a_W T_W + b \tag{12}$$

All the coefficient terms i.e. a_P, a_E, a_W denote the ratio of $\frac{k}{\delta_x}$ and, b represents the source term, $\bar{S}\Delta x$. By combining all sets of discretization equations obtained from going through each grid point into a tri-diagonal matrix, the solution can be easily solved using the techniques of linear algebra, such as by Gaussian Elimination. Note that in some cases, the source term can be of a function of T. In order to account for this, it is convenient to linearize the term into the form shown as follows.

$$\bar{S} = S_c + S_P T_P \tag{13}$$

where S_c stands for the constant part of the source and, S_P is used as the coefficient for the T_P (not necessarily the temperature at point P. Rather, it is an assumption that such a value prevails throughout the simulation domain.) This is the concept of the stepwise profile assumption that was mentioned before. It is important to keep in mind that it is free to use both profile assumptions for a given governing equation i.e. piecewise for the $\frac{dT}{dx}$ and stepwise for the $\bar{S}$, for whichever gives the best qualitative description [26].

1.3.3 Boundary Conditions

In all CFD simulations, boundary conditions play a crucial role, as the value may be that of the value of interest i.e. the temperature at the surface where the temperature can't be measured, or, the values are known, and this can be used to solve the profile distribution. In all cases, there always exist one extra grid point that lies outside of each boundary of the simulation domain occupying only half of the control volume. If the values are already known, no specific equation is required. Nevertheless, if the values are unknown, then it is necessary to construct another set of discretization equation at any point of interest (T_B for example in the 1D problem shown in Figure 1.14. The equation is obtained in the similar fashion as for other grid points, but this time, one only integrates through half of the control volume [29].

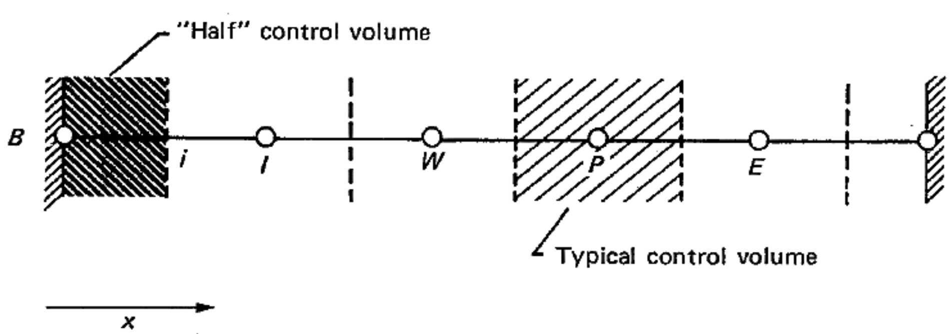

Figure 1.14 Boundary conditions-half control volume

1.3.4 Unsteady State Condition with Explicit, Crank-Nicolson and Fully Implicit Schemes

The example above is a steady state question. However, in the real world, most thermal conduction problems are time dependent, for which the governing equation is;

$$\rho c \frac{\partial T}{\partial t} = \frac{\partial}{dx}\left(k \frac{\partial T}{\partial x}\right) \tag{14}$$

It is convenient to denote all temperatures at the previous time t as T_P^0, T_W^0, T_E^0, and the new temperatures at time t+Δt, T_P^1, T_W^1, T_E^1. The integration over the control volume would be as follows;

$$\rho c \int_w^e \int_t^{t+\Delta t} \frac{\partial T}{\partial t} dt dx = \int_t^{t+\Delta t} \int_w^e \frac{\partial}{dx}\left(k \frac{\partial T}{\partial x}\right) dx dt \tag{15}$$

It is safe to assume that the value of temperature prevails throughout the control volume at any given time, hence the left-hand side of equation 15 can be written as followed.

$$\rho c \; \Delta x (T_P^1 - T_P^0) = \int_t^{t+\Delta t} [\frac{k_e (T_E - T_P)}{(\delta x)_e} - \frac{k_w (T_P - T_W)}{(\delta x)_w}] \; dt \tag{16}$$

Note that to evaluate the integral on the right-hand side, assumption has to be made to evaluate how T_P T_w T_E vary with time. To do this, the weighting factor (Eq.17) is introduced.

$$\int_t^{t+\Delta t} T_P \; dt = [f T_P^1 + (1-f) T_P^0] \Delta t \tag{17}$$

The value f has a range from 0 to 1, depending on the condition given, the value can be adjusted accordingly. With this in mind, the discretization equation obtained by evaluating the integrals in eq.15 can be written as follows;

$$\rho c \frac{\Delta x}{\Delta t}(T_P^1 - T_P^0) = f\left[\frac{k_e(T_E^1 - T_P^1)}{(\delta x)_e} - \frac{k_w(T_P^1 - T_W^1)}{(\delta x)_w}\right] + (1-f)\left[\frac{k_e(T_E^0 - T_P^0)}{(\delta x)_e} - \frac{k_w(T_P^0 - T_W^0)}{(\delta x)_w}\right] \tag{18}$$

This equation can be re-arranged as previously shown by replacing and grouping terms

$$a_P T_P = a_E[fT_E + (1-f)T_E^0] + a_W[fT_W + (1-f)T_W^0] + [a_P^0 - (1-f)a_E - (1-f)a_W]T_P^0 \quad (19)$$

If f = 0, the discretization equations become the explicit scheme, f = 0.5 leads to the Crank-Nicolson scheme, and with f = 1, the fully implicit scheme. In the explicit scheme, the assumption is made that the temperature value remains the same throughout all the control volume at time t and is only subject to change at t+Δt. In the fully implicit scheme, the assumption is that there is a sudden change of temperature from T_P^0 to T_P^1 and remains at T_P^1 for that whole-time step. As for the Crank-Nicolson scheme, the Temperature has a linear variation relationship to the time. For most cases, in order to not violate any condition and obtaining unrealistic results, the fully implicit scheme appears to be the most reasonable, since under most of the circumstances it avoids getting negative coefficient. It is found that negative neighbor coefficient can lead to the situation that an increase in boundary temperature results in a decrease in the adjacent point and that is physically unreasonable. For the fully implicit solution, with f = 1, regardless of the size of the time step, this situation can be avoided as the coefficient of T_P^0 will never be negative. Although in many other cases, the Crank-Nicolson scheme can be more accurate with smaller time steps as it gives a nice linear profile. However, that accuracy drops significantly with increasing time step size, as the curve exhibits an exponential decay behavior. Later on, in most of the modern CFD techniques, the two schemes are combined, so as to enhance the calculation result. That is called the exponential scheme [26, 27].

1.3.5 2D Situation

In terms of the two and three-dimensional setups, the general rule is the same, except there exist more neighboring grid points that need to be taken into account, in order to obey the conservation law. A typical 2D grid can be seen in Figure 1.15 below. Different from the 1D situation, there are more interfaces that need to be included into the discretization equations i.e. the north and south grid points with additional length of Δy.

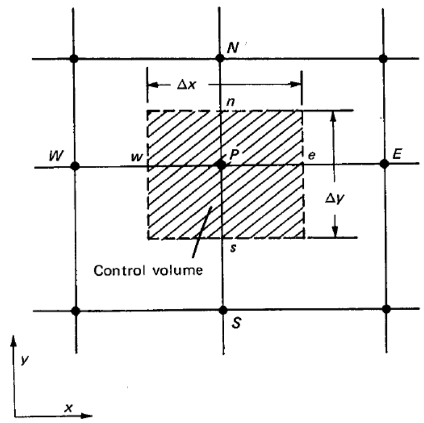

Figure 1.15 2D grid point cluster and control volume

The governing differential energy equation and its corresponding discretization equation look like the following with N denoting north, and S denoting south.

$$\rho c \frac{\partial T}{\partial t} = \frac{\partial}{\partial x}\left(k\frac{\partial T}{\partial x}\right) + \frac{\partial}{\partial y}\left(k\frac{\partial T}{\partial y}\right) + S \tag{20}$$

$$a_P T_P = a_E T_E + a_W T_W + a_N T_N + a_S T_S + b \tag{21}$$

1.3.6 Solution Methods for Algebraic Equations

Conventional Gaussian elimination method can be employed to solve a system of algebraic equations. In a one-dimensional situation, due to its particular constructing method of equations, this matrix forms a special Tri-Diagonal Matrix algorithm (TDMA) that can be easily solved either analytically or numerically, depending on the size of the matrix [30]. Nevertheless, this TDMA can be difficult to be apply for multi-dimensional problems. For linear problems, which are required to be solved only once, they can be approached with a direct method. When it comes to non-linear problems, the direct method (TDMA) can be complicated as it requires lots of storage memory to store values necessary to update the field. One of the most popular methods to tackle these problems is the iterative method. This technique requires a first guess of the field of the dependent variables (T for example in the energy governing equation). These values will then be updated successively to reach improved field until it is sufficiently close to the correct solution to the derived algebraic equations. Two of the most commonly seen iterative methods are the Gauss-Seidel point by point and the line by line method [31].

With the Gauss-Seidel method, only one set of T's will be stored in the memory. These values can be from the first initial guess or the values from the previous iteration. Given a general algebraic equation as shown with nb denoting any neighboring point.

$$a_P T_P = \sum a_{nb} T_{nb} + b \tag{22}$$

The value of interest T_P can then be calculated

$$T_p = \sum \frac{a_{nb} T_{nb}^{*} + b}{a_P} \tag{23}$$

T_{nb}^{*} here stands for the neighboring point value previously stored in the computer. For any grid point that has been visited during the iteration, the freshly calculated value will replace the previous one. For the ones yet to be visited, the value stored here remain the same as from the previous iteration. Once all grid points are visited, one iteration for the Gauss Seidel method is completed. For the solution to meet a desired standard i.e. converged, a criterion is constructed by Scarborough [32].

$$\frac{\sum |a_{nb}|}{|a_P|} \leq 1 \; for\ all\ equations\ \ or \tag{24}$$

$$\frac{\sum |a_{nb}|}{|a_P|} < 1 \; for\ at\ least\ one\ equation$$

One major drawback of the Gauss Seidel method is that the computation time can be really long, if the simulation domain involves a large amount of grid points. The reason is obvious, since for the Gauss Seidel method, it transmits the boundary condition values at a rate of one grid point interval, for each successive iteration. Hence, to overcome this issue, a new method, line-by-line method, was invented by combining the direct method (TDMA), with Gauss Seidel. Figure 1.16 below shows a schematic diagram of the line-by-line method.

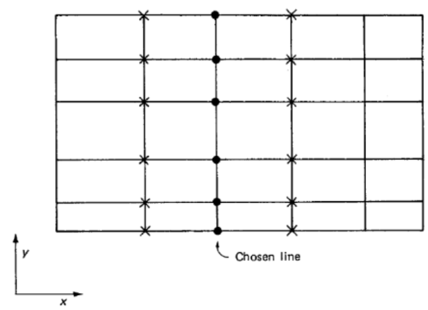

Figure 1.16 line-by-line iteration method

Instead of going through each grid point one by one, a line is chosen that crosses the grid points along same row or column, i.e. in either x, y or z direction (shown by the dotted line in the above figure). It assumes that all values are known on its neighboring grid points (lines with cross). This allows the problem to be turned into a similar construction as for the 1-D algebraic equations, that can be easily solved with TDMA. Additionally, the computation time can be significantly reduced since it takes much shorter time to transmit all boundary condition information to the interior simulation domain [26].

1.3.7 Previous Applications

As mentioned previously, CFD modeling has been used quite extensively in process metallurgy to help in designing and optimizing processes. One example are the studies of the effect on fluid flow and solidification mechanisms when using different Submerged Entry Nozzle (SEN) in the TRC process. Another important aspect of TRC process that was also studied with the aid of numerical models is the relationship between the interfacial heat flux and the casting speed. Needless to say, the delivery system, being an important part of the HSBC process, is also studied to acquire better understandings toward the fluid flow and heat transfer phenomena, in order to come up with optimal configurations [15].

2. Chapter 2 Analysis of As-cast AA5182 strips produced via MMPC Pilot-Scale Horizontal Single Belt Casting (HSBC) Process

2.0 Introduction

Horizontal Single Belt Casting (HBC) process is a novel near net shape strip casting technology currently under development. This manufacturing method features a very compact process line which, in turn, translates into lower capital and production costs, compared to conventional production methods. Due to this, it is foreseeable that this technology will gain significant attention in the coming years from industries where metallic sheets are essential products. Until now, the production of aluminum alloys metallic sheets requires significant outlays of cost and energy. For this reason, most of the automobile companies still face challenges in achieving the goal of transitioning to a higher percentage use of light metals. With the gradual success of the HSBC process, it is believed that those industries can greatly benefit from this new technology.

In this chapter, the as-cast AA5182 strips produced from the pilot scale HSBC process were analyzed. For the current experimental setup, a 45^{o} inclined refractory ramp was installed immediately beneath the delivery system, in the hope of achieving better fluid flow behavior. The microstructure, porosity, secondary phases, and the surface quality, were all studied, so as to evaluate the strips' quality coming from the current setup. The distribution of porosity and its tendency to form, were analyzed using the images taken from an optical microscope, and later processed with ImageJ. Scanning Electron Microscopy (SEM), as well as Back-Scattered Electron (BSE) microscopy, were conducted to study the secondary phases present in the alloy. Lastly, the surface quality was studied using 3D laser profilometry.

2.1 MMPC Horizontal Single Belt Casting (HSBC) Process. Overview and Experimental Procedure

2.1.1 Materials Preparation and Melting Operations

Figure 2.1 illustrates the physical setup and also the schematic diagram of the pilot-scale MMPC Horizontal Single Belt (HSBC) system. This casting machine was utilized to produce the 200 mm and 250 mm wide AA5182 strips with an averaged thickness of 5.65 mm.

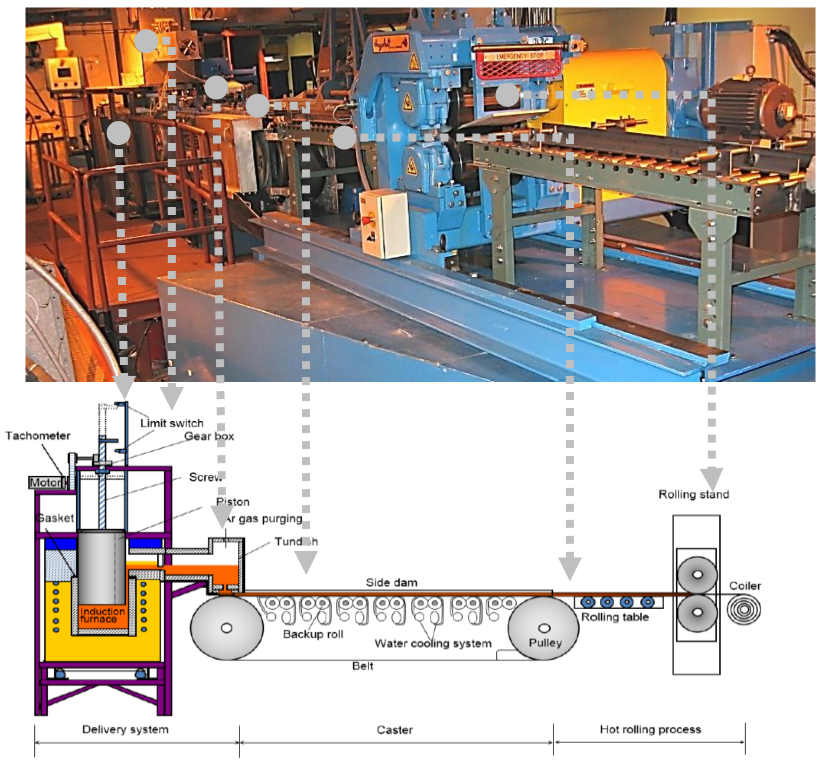

Figure 2.1 Pilot scale MMPC-HSBC machine operating at MetSim Inc., Montreal.

Before the casting operations, roughly 80 kg of the alloy was prepared using pure aluminum ingots, master alloys of Al-25wt%Mg, and Al-25wt%Mn. The theoretical and the actual compositions of the final strip products are shown in Table 3 below. (The compositions were analyzed using IR Spectroscopy spark tests)

Table 2-1 Chemical composition of AA5182-Theoretical and Actual wt.%

Theoretical	Al	Mg	Mn	Fe	Si
Weight %	*93.2 – 95.8*	*4.0 – 5.0*	*0.2 – 0.5*	*<0.35*	*<0.20*
Actual Sample 1	Al	Mg	Mn	Fe	Si

Weight %	*94.71*	*4.636*	*0.301*	*0.111*	*0.069*
Actual Sample 2	Al	Mg	Mn	Fe	Si
Weight %	*94.71*	*4.571*	*0.371*	*0.108*	*0.067*

Before melting, the 500 lb capacity induction furnace (Figure 2.2) was first pre-heated to achieve desired interior temperature, i.e. around 700°C. After the temperature was reached, the gas-burner was then switched off, and materials were charged in to the furnace for inductive heating, and melting. The alloying sequence usually goes from melting the pure aluminum ingots first, followed by the addition of aluminum-manganese, and lastly the aluminum-magnesium. Mn was added first due to its relative higher melting point than Mg. After all materials were melted, the induction heating system was then adjusted accordingly to have the bulk temperature stabilizing at 690°C. This temperature, which was much higher than the liquidus temperature of AA5182, was selected for two reasons. Firstly, it was to account for heat loss when transferring the furnace to casting position. Secondly, it was to ensure that when the melt entered onto the moving belt, its temperature would be roughly 15°C above the liquidus temperature (15°C superheat).

Figure 2.2 Induction furnace

Finally, the melted alloys went through the degassing process, and that was followed by the addition of Al-Ti-B master alloy. During the degassing step, argon gas was used to rid the melt of hydrogen dissolved into the melt. The hydrogen can be absorbed from reactions with water vapor within the air. Thus, aluminum has the tendency to react with water vapor to form alumina, and hydrogen atoms ($\underline{H}$) that dissolve into the molten bath. At higher melt temperatures, the solubility of $\underline{H}$ atom was high, however, the solubility dropped as the alloys undergo solidification [33]. As a result, the hydrogen was rejected and escaped from the Al-matrix, leaving little voids within the structure. This porosity would negatively affect the mechanical properties of the material. Hence degassing was essential.

As for the purpose of the Al-Ti-B addition, it acted as a grain refiner by reducing the α-Al grain size. The mechanism for this grain size reduction is thought to be either by restricting the grain growth at the nucleation sites for α-Al (pinning mechanisms of TiB_2 compounds), or by increasing the α-Al nucleation density. Either of these mechanisms ensure that while the alloy undergoes solidification and crystallization, the grain size and it would make post-casting processing such as rolling and extrusion much easier [34].

2.1.2 Delivery System Installation & Belt Preparation

Figure 2.3 shows the schematic diagram of the delivery system's setup. The delivery system was composed of 3 troughs, as illustrated below. The exiting nozzle was located at the end of trough #3. The detailed design of the head box (trough 3) can be found in Figure 2.4.

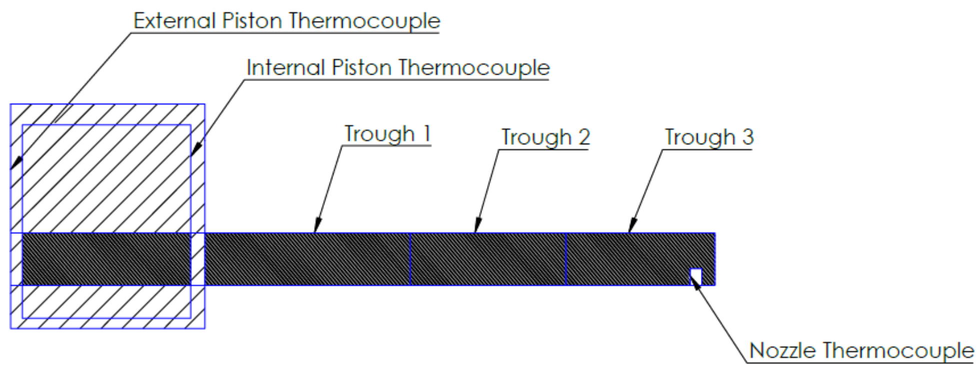

Figure 2.3 Delivery/feeding system

The detailed design of the nozzle/feeding system is shown in Fig.2.5. For all pilot scale experiments, an 45° inclined refractory ramp was attached immediately below the exiting nozzle to allow the molten alloy to fall first onto the ramp, and then, on to the moving water-cooled belt made of steel.

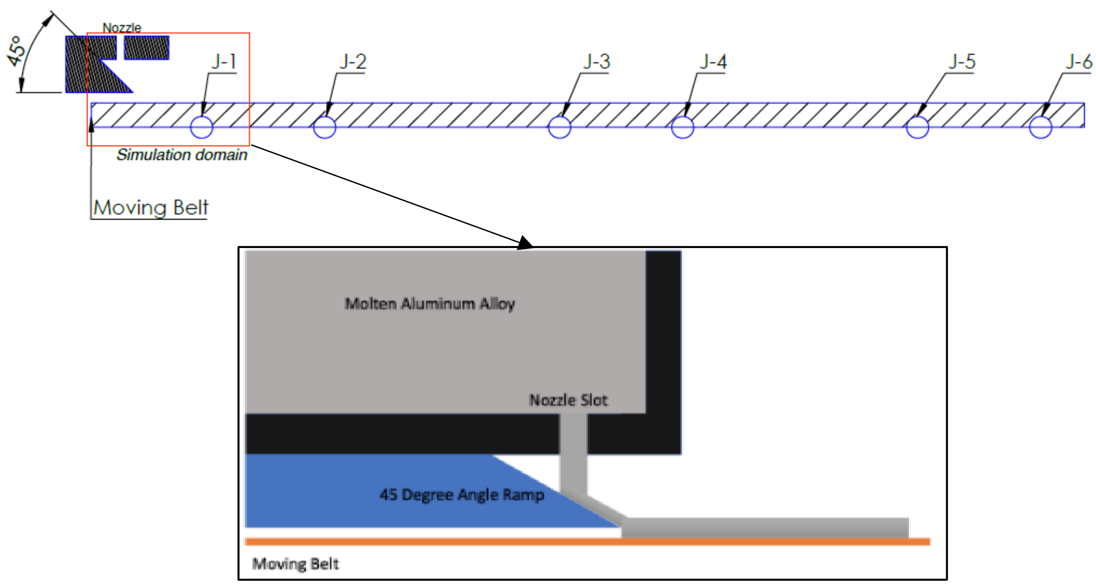

Figure 2.4 Inclined feeding system-nozzle configuration

Once all troughs were installed properly and leveled, a thin layer of boron nitride coating was then applied to the interior surface of the delivery system and the piston's exterior surface. The purposes were to prevent melt sticking and to protect all components against high temperature. Additionally, for the belt, graphite spray was applied to enhance the smoothness of the surface, as well as to ensure better contact between the molten alloy and the belt.

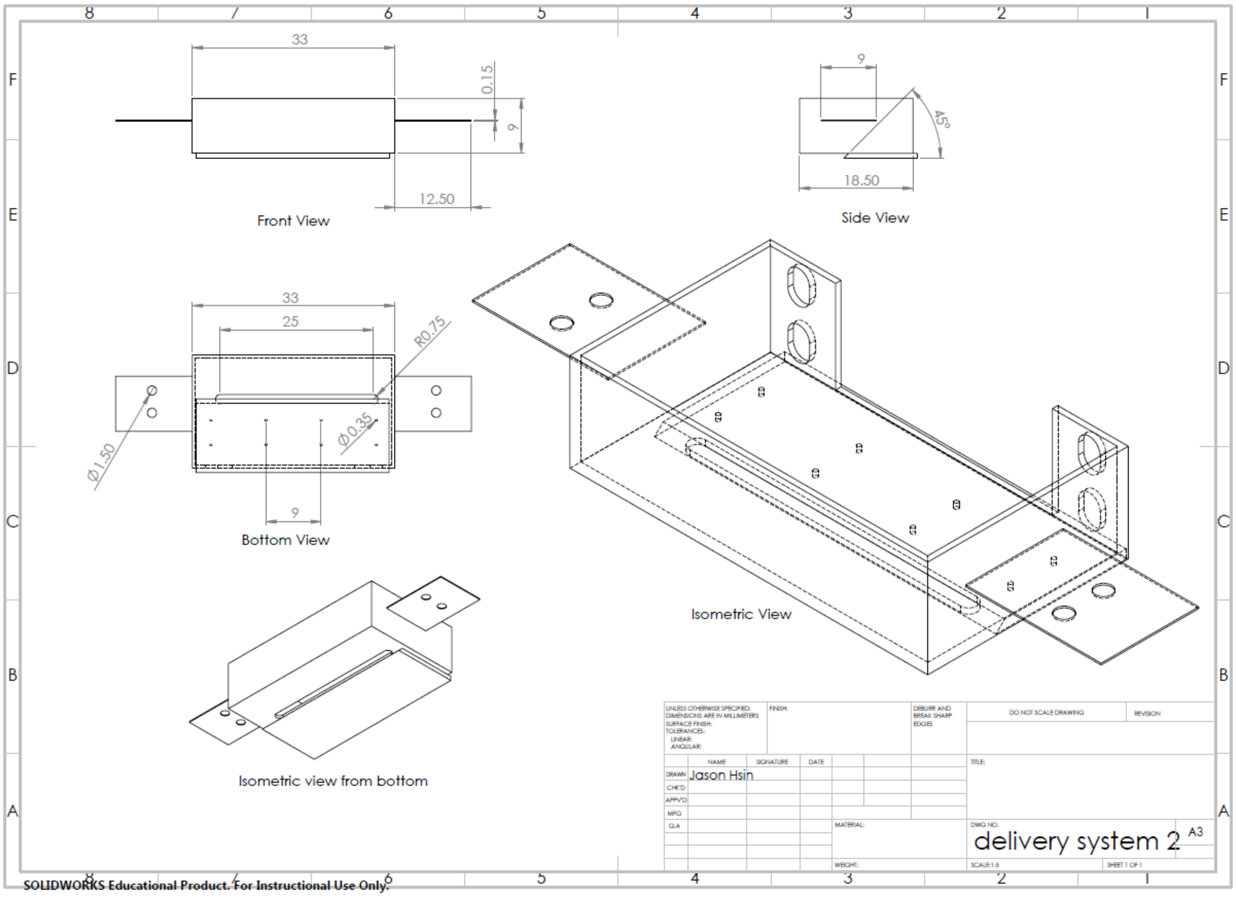

Figure 2.5 Head box (trough 3) of the delivery system

In order to keep better track of the temperature evolution, each trough had two k-type thermocouples inserted. The reason for having two each was because the electrical preheater used for pre-heating the delivery system required one upper and one lower limit readings, in order to ensure steady heating. As for the belt's temperature recording, 8 J-type thermocouples were installed underneath it and distributed in the manner shown in Fig.2.4. All temperature data were acquired using Dasylab with the work chart shown in Fig.2.6. Each channel was connected to specific component of the delivery system. Details can be found in table 4.

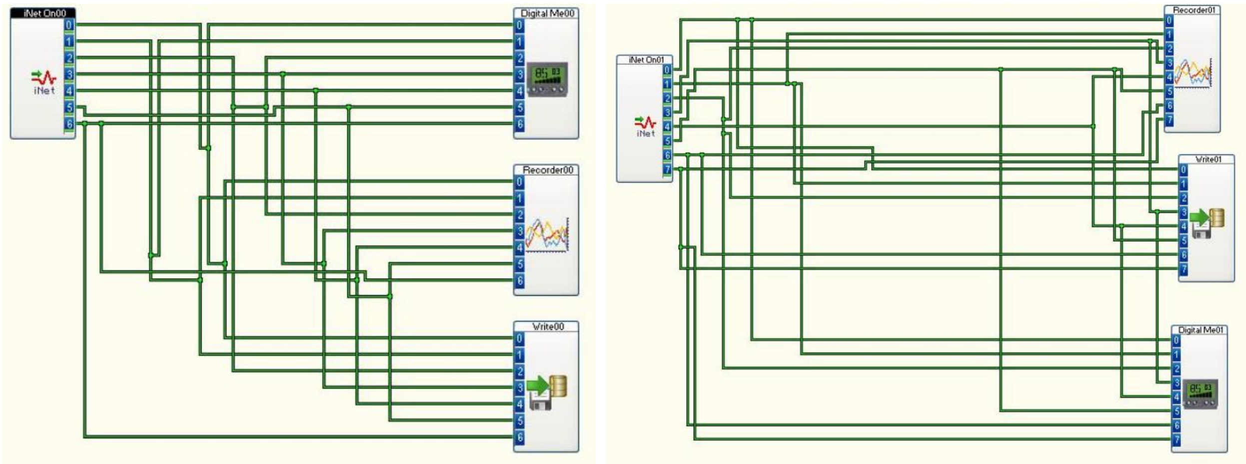

Figure 2.6 Dasylab worksheet for temperature recordings

Table 2-2 Dasylab channels and its corresponding measuring locations

Instrunet # : connecting channels : pilot caster labeling	Correspondent
0 : (channel 1) : 1	Trough 1
1 : (channel 4) : 2	Trough 2
2 : (channel 7) : 3	Trough 3
3 : (channel 10) : 4	Piston preheater
4 : (channel 13) : 8	Trough 1 (second measure)
5 : (channel 16) : 7	Nozzle (Trough 3)
6 : (channel 19) : 6	Trough 2 (Second measure)

Noted that AA5182 aluminum alloy has a liquidus temperature of 638^{o}C. To produce this strip via the HSBC process, at least 15^{o}C superheat was required, i.e. 653^{o}C, to avoid early solidification, and to ensure a high temperature gradient for rapid cooling. During the casting experiments, the actual temperature readings of the molten alloys right before it touched the water-cooled moving belt, were found to be within the range of 653^{o}C ~ 658^{o}C. As for Troughs 1, 2 and 3, the temperatures achieved after pre-heating were 448^{o}C, 605^{o}C and 501^{o}C respectively. Finally, for all experiments, the water temperatures at all locations of the belt were maintained at 25^{o}C at all times.

2.1.3 Casting Operations

Once all preparations were done, the induction furnace containing the molten alloy at 690ºC was moved to the casting position using a hand-driven chain system. To lift the furnace and connect it with the delivery system, four hydraulic pistons placed at the four corners of the furnace platform were used. The melt was then displaced by the piston's downward motion, so as to fill up the delivery launder. Finally, fluid was displaced upwards, into the launder, and reached a suitable height. The Stopper Slot was lifted from the slot nozzle, and the AA5182 alloy metal poured through the nozzle onto the moving belt, running at a speed of 24m/min. The piston's speed was pre-determined using Bernoulli principle in order to maintain constant metal head in the launder, so as to ensure the thickness of the cast strip was uniform. During casting, belt speed could be adjusted, so as to maintain the hydrodynamic pressure (metal head) constant, and to prevent overflow. To produce strips with different width i.e. 200 mm and 250 mm, different exiting nozzles were tailored, and the piston's speed was re-calculated according to Bernoulli Equation. Some

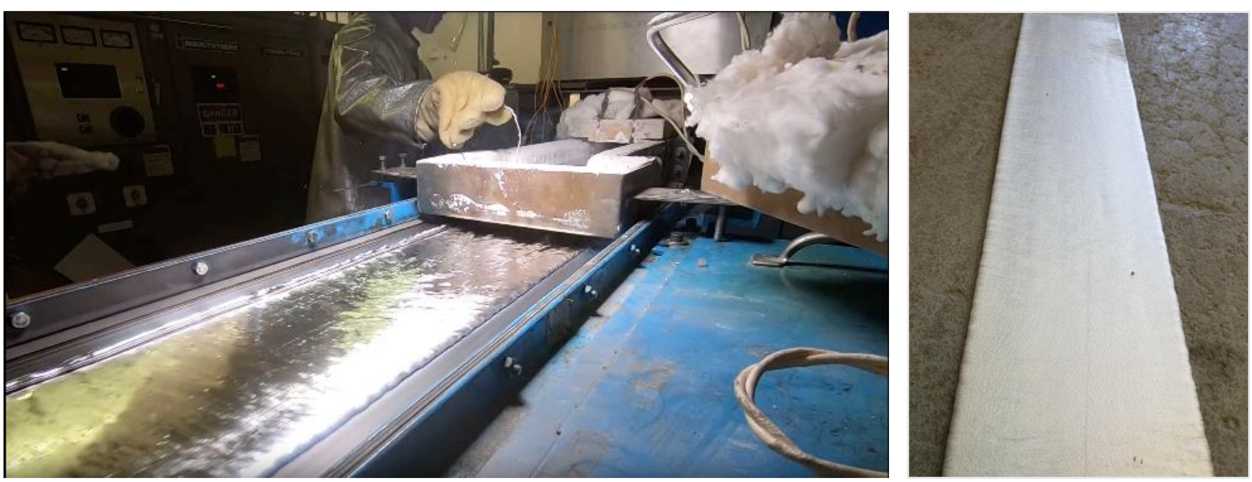

Figure 2.7 left: casting operation, right: as-cast AA5182 strip

attempts were made to hot roll the as-cast strip to thinner thickness, using limited water cooling of the strip ahead of the pinch roll /mini-mill. Unfortunately, this was insufficient, so that all the segments hot rolled, experienced thermal shock induced cracking. As the re-location and water-cooling segments needed further design work, hot ductility tests were conducted, so as to determine the best hot rolling temperature, and position for re-location of the pinch roll. These results will be discussed in Chapter 4.

2.2 Porosity Distribution Analysis of HSBC As-Cast Strips

Porosity has always been one of the major defects in casting operations, as it can severely compromise the mechanical properties of the final products. These voids (porous structure) can appear in the aluminum alloys microstructure due to various reasons. The most publicly accepted theory for conventional DC, TR and TBC casters, is that the main mechanism for the formation of porosity is caused by solidification shrinkage, and non-feeding of liquid metal to make up the deficit. This is often combined with gas segregation and precipitation. For the as-cast strips produced via the MetSim HSBC caster, the porosity distribution was studied sectionally in the direction parallel to the heat flux. The procedures and results are presented below.

2.2.1 Procedure for Porosity Measurement

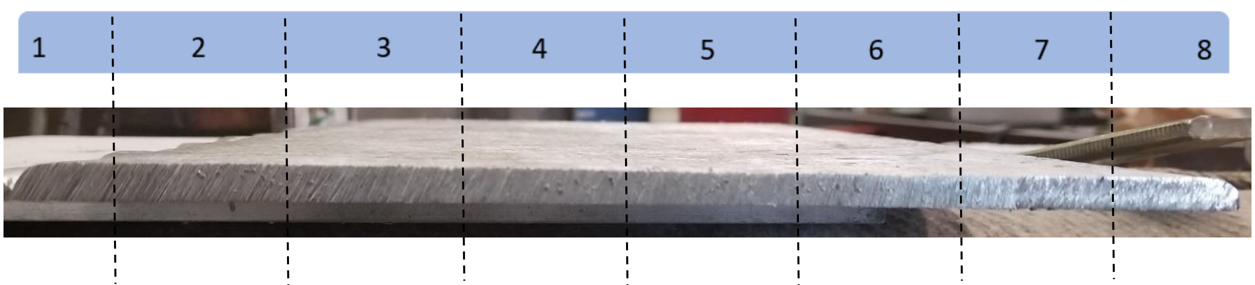

Figure 2.8 Sampling method for porosity analysis

In order to measure porosity, the HSBC as-cast strips were cut to expose its cross-plane section that was normal to the casting direction (Figure 2.8). The segment was further divided into 8 pieces as shown in the schematic diagram. Each cut sample was prepared using general mounting, grinding and manual polishing procedures, in order to reveal the pores. Once finished, optical microscopy was performed to take images at the top, middle and bottom sections of each sample. The images, shown in Figure 2.9 for example, were analyzed using ImageJ software, so as to measure the area fraction. The initial micrograph was first changed into 8-bit and cropped in order to remove the scale bar and any shading caused by surface imperfections. The brightness/contrast was then adjusted manually to differentiate the pores from its surrounding. The threshold was then applied to separate the pores from the background. Once the threshold was applied, the analyze particles function was used to determine the area fraction. This procedure was done on both AA5182 and AA2024 as-cast strips produced from the MMPC HSBC caster to show the comparison.

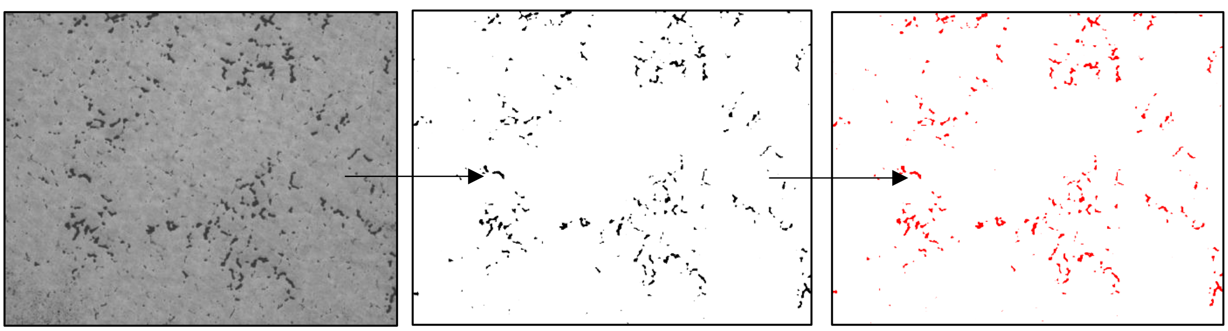

Figure 2.9 Image processed with ImageJ for porosity calculation

2.2.2 Results & Discussion

The results are plotted and shown below. It is established that the heat flux and temperature gradients do play important roles in determining the amount of porosity formation. It can be seen in Figure 2.10, that the middle section of the strips has a relatively higher volume fraction of porosity as compared to other parts, whilst the bottom section had the lowest volume fraction.

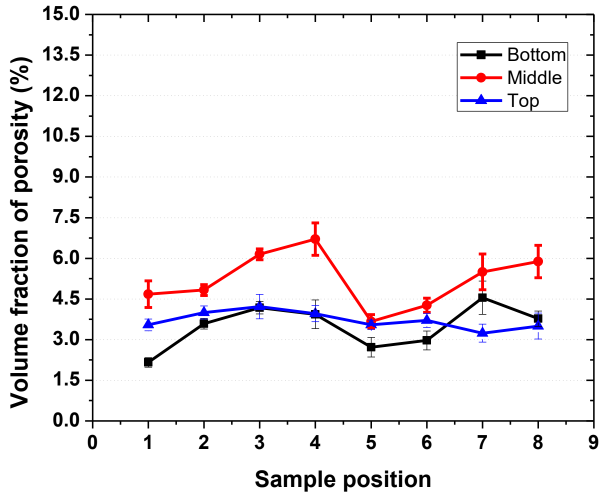

Figure 2.10 Volume fraction of porosity with respect to the positions

The trend can be reasonably related to the heat flow within the strips during the solidification process. The bottom surface that was in direct contact with the continuously water-cooled steel belt experienced a higher heat flux, which provides for a higher density of nucleation sites. The dendrites originating from these densely packed nuclei can form a more refined grain structure, which in turn, creates smaller Secondary Dendrite Arm Spacing (SDAS). As has already been proven through many experimental research results [35-37], pores exist mostly within the gap between neighboring secondary dendrite arms at regions close to surfaces. The smaller the SDAS, the size and numbers of pores can be significantly reduced. In the case of the top surface, even though it was furthest away from the moving belt, it was also allowed to be air-cooled since it was exposed to open air. The air-cooling rates was not as good as the water-cooling, nevertheless, it might have been sufficient enough to restrict the amount of porosity present in the structure. Lastly, the porosity level measured in the middle sections exhibit the highest porosity, but this may have been caused by instabilities in the falling stream onto the first point of impingement on the sloped refractory, causing microbubble formation within the strip. In addition, by comparing the three images taken at different regions (Figure 2.11), it is observed that the pore's shapes are more irregular and larger in size at the middle layer. Rather than forming just between the secondary dendrite arms, pores also exist in between primary dendrites, hence causing the pores to take on more irregular shape i.e. shrinkage pores.

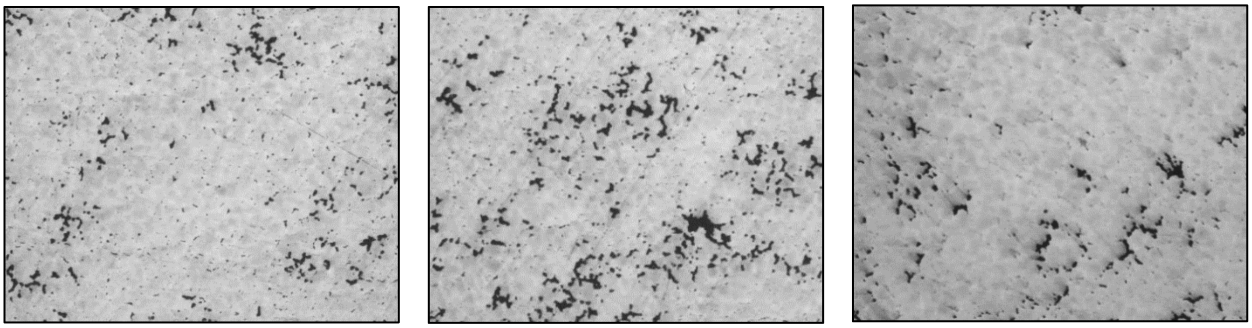

Figure 2.11 left: bottom section, middle: middle section, right: top section

Last but not least, special attention was paid to the porosity condition at the top and bottom surfaces of the strips (fig. 2.12). Pores forming right on, or too close to, the surface can have detrimental effects when the strips go through post-processing steps such as rolling. The images shown below were taken under higher magnification (100x) to reveal the structure.

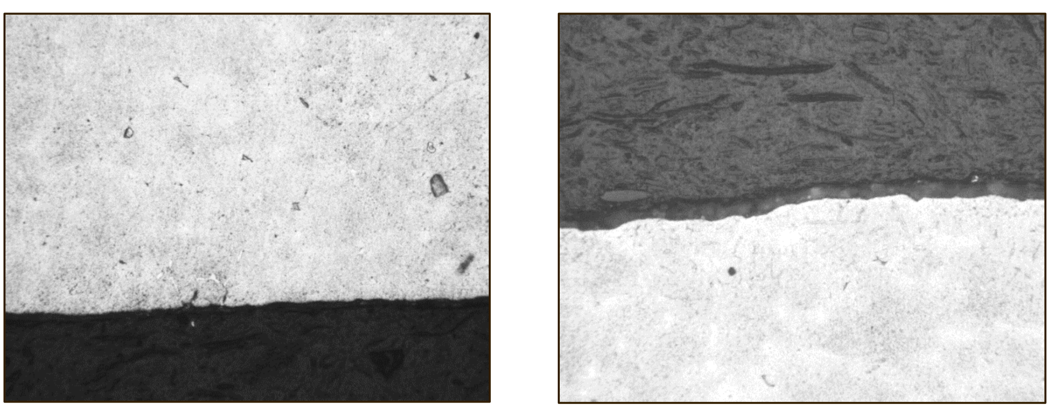

Figure 2.12 left: bottom surface, right: top surface

It is observed that on both surfaces, the number of pores is close to none and that is owing to the high cooling rates that the HSBC process is able to achieve. Hence, downstream processing should not be a problem. A similar method of analysis was applied to study the trend in porosity distribution for AA2024 strips produced with the same MMPC-HSBC caster. The rough data suggested that the porosity level of AA5182 is slightly higher than the AA2024 at the middle section of the strips, using the same two impingement delivery system.

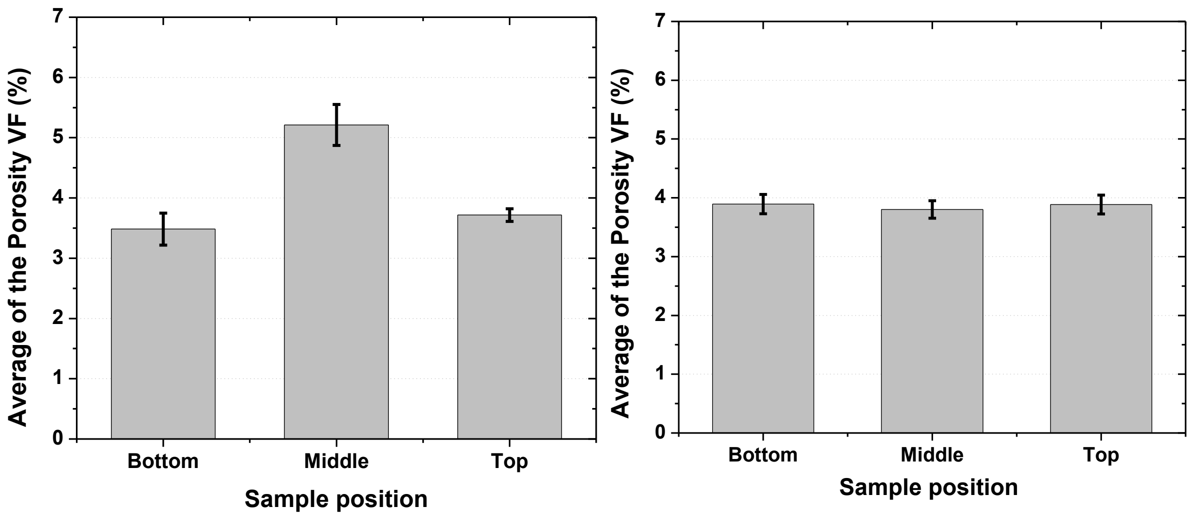

Figure 2.13 Average porosity comparison- left: AA5182, right: AA2024

There is no direct evidence that can relate this difference to the HSBC process since for the top and bottom sections, the porosity distributions were similar. A possible explanation would be due to the different composition of the materials. For AA5182 and AA2024, the magnesium content is

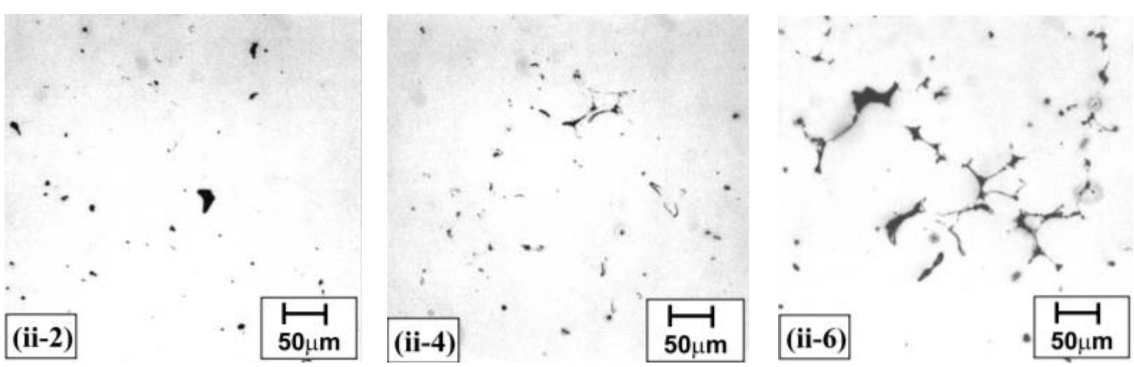

Figure 2.14 As-cast AA5182 DC slabs with left: 2wt.% Mg, middle: 4wt.% Mg, right) 6 wt.% Mg

4.0~5.0wt% and 1.2~1.8wt% respectively. P.D. Lee et al [36] at Imperial College had conducted experiments to investigate the relationship between magnesium content and the characteristic of porosity found in DC cast aluminum-magnesium alloys. Similar cooling rates were applied to solidify three DC cast slabs of aluminum, containing 2, 4 and 6 wt.% Mg. The samples were prepared and then analyzed using optical microscopy. The resulted micrographs obtained by them are shown above (Figure 2.14).

All three images were taken at the same location i.e. 60mm away from the surface of the ingots. It is clearly seen that with increasing levels of magnesium, the amount and size of pores increase dramatically. It was found that Mg has the tendency to increase the hydrogen absorption. The 6 wt.% of Mg ingot has almost twice the level of hydrogen found than the one with 2 wt.% Mg, hence leading to a higher porosity level after solidification. The relationship was plotted and shown in Figure 2.15. According to their research [36, 38], the in-line rotatory degasser was used. Nevertheless, it had very little effect in getting rid of dissolved hydrogen for alloys with high magnesium content. The same situation was thought to be taking place during the HSBC process, and that is believed to be the major factor contributing to this distinct difference between the two alloys. It is however interesting to see that at the regions close to the surfaces i.e. the top and bottom sections, the porosity levels are almost identical. This is owing to the efficient cooling mechanism (short solidification time) of the HSBC process. The problem with hydrogen dissolution was able to be overcome whilst the porosity level is independent of the magnesium level in those regions where local cooling is adequate.

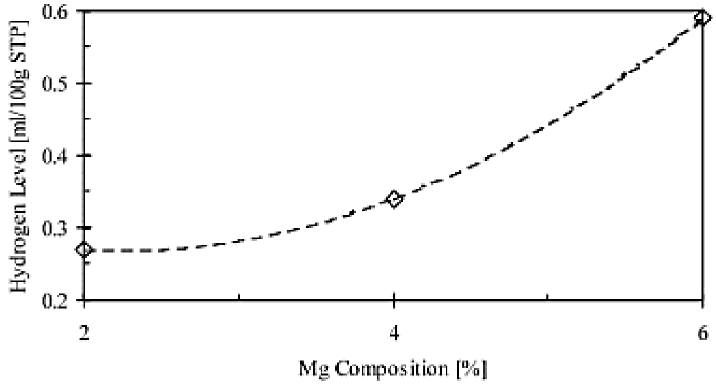

Figure 2.15 Hydrogen level vs Mg composition (wt.%) [37]

2.3 Grain Size Measurements

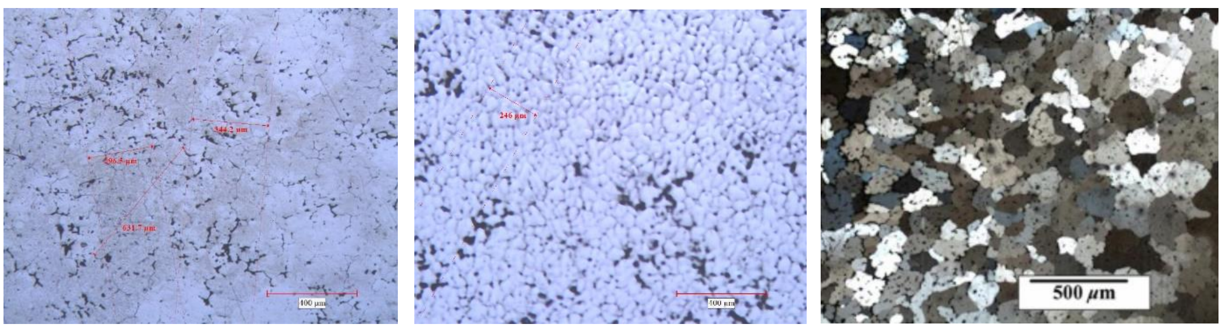

Figure 2.16 left: as-cast AA5182 HSBC microstructure etched with HF solution, middle: as-cast AA5182 HSBC microstructure with electro-polishing, right: as-cast AA5182 DC samples (surface)

Grain size plays crucial role in metallic materials as it is one of the main factors that affect the mechanical strength. It is therefore important to evaluate the grain structure of the as-cast AA5182 HSBC strips. To do this, the same samples prepared for porosity analysis were etched with 5 vol% HF + ethanol solution, to reveal the grain boundaries. The average grain size at all locations measured by the linear intercept method was found to be 63.1μm ± 7.8μm. Figure 2.16 shows the grain structure of samples under the optical microscopy with 50X magnification. The image in the middle shows the samplse that were electro-polished using perchloric acid. This method is excellent for revealing the grain boundaries and was used to further validate grain sizes.As can be seen, the grain morphology of the HSBC as-cast strip is similar to that of the DC AA5182 slab's grain structure (Figure 2.16 right) taken from the section where the interfacial cooling is the highest, i.e. the surface of the ingot. However, the HSBC strip's grain size is in fact much smaller compared to the DC samples, which has the average grain size of 123μm ± 20μm as found by N. Jamaly et al [39]. The reason for such a huge difference is due to the high cooling rates that the HSBC process is able to achieve. As the grain size of the as-cast products is already smaller, i.e. almost half of those found in DC ingots, the number of post-processing steps can be reduced to achieve the targeted strength and microstructure required for its applications.

Similar experiments were done using the HSBC simulator developed by the MMPC, which is much smaller in size, but is very efficient in mimicking pilot scale casting operations. The microstructure is shown in Figure 2.17. The average grain size measurements appeared to be in a similar range, i.e. 60.2μm ± 8.2μm, as the strip's microstructure produced via the pilot scale HSBC machine. With higher magnification (100X) and deep etching, the secondary dendrite arm spacings (SDAS) were found to be roughly 7μm ± 2μm (Figure 2.17). In terms of the heat flux measuremnent (Figure 2.18), the peak value was calculated to be 2.2MW/m^2, which falls quite reasonably into the heat flux ranges constructed by Dr. Donghui [40]. Hence, based on these findings, the HSBC process is proven to be capable of producing high quality as-cast AA5182 strips, and probably many other advanced alloys for the transportation industries.

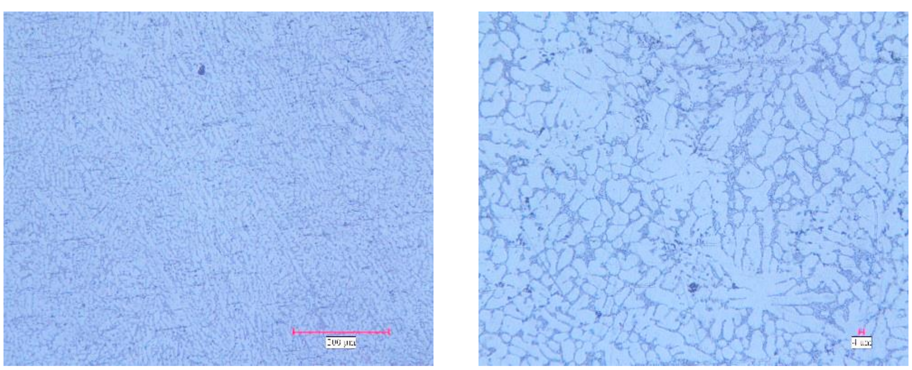

Figure 2.17 Microstructure of as-cast AA5182 HSBC strip with simulator

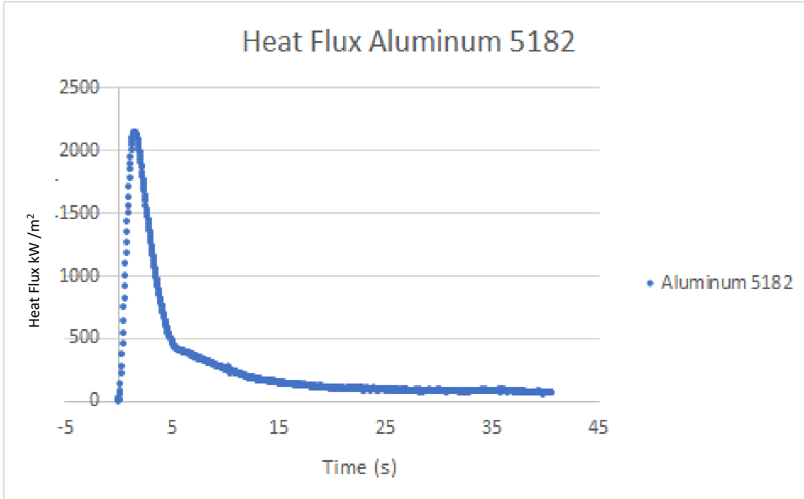

Figure 2.18 Heat flux from the simulator

2.4 Analysis of Secondary Phase of HSBC as-cast Strip using Scanning Electron (SEM), and Backscattered Electrons (BSE) Microscopy

Conducting an analysis of the intermetallic compounds found within the HSBC as-cast strip can provide useful information, as the secondary phases and local cooling rates are inter-related. For AA5182 alloys, the most commonly found dominant phase are the iron-bearing eutectic particles. These iron-rich particles can be further categorized into two types, namely the Chinese script $Al_m(FeMn)$, and the platelet-like $Al_3(FeMn)$, or $Al_6(FeMn)$. It is experimentally proven that with increasing cooling rates, the platelet-like structure $Al_3(FeMn)$ or $Al_6(FeMn)$ that precipitated at much lower cooling rates can be replaced by $Al_m(FeMn)$. Here "m" has a range from between 4.0 to 6.0. In theory, the $Al_m(FeMn)$ phase is much preferred as it has less harmful effect toward the mechanical properties. The $Al_3(FeMn)$ particles on the other hand, feature a needle-like morphology, making them more brittle as they tend to act as stress concentrators. [23, 25]. The images were taken using SU3500 Scanning Electron Microscope (SEM) and the results are shown below (Figure 2.19, 2.20, 2.21) with the corresponding chemical compositions of iron-bearing particles identified and expressed in terms of atomic weight percentage (At%) (Table. 2-3). It is clearly seen that at the bottom section where the cooling is most efficient, the dominant iron-bearing particles are the $Al_m(FeMn)$. These particles are much smaller in size and possess the preferred Chinese script structure, hence making the alloys much stronger. For accuracy, multiple points were selected on all samples. It was found that less than 20% of the iron bearing particles are the platelet-like $Al_3(FeMn)$ particles, and that these were owing to the high cooling achieved by the HSBC process. On the top and middle sections, the dominant phase is $Al_m(FeMn)$. Further, the relative amount drops slightly to 70% for the cooling rates at these regions were a little less compared to the bottom. Nevertheless, the amount still remains quite high, suggesting that the cooling rates is still rather consistent throughout the whole thickness of the HSBC as-cast strips.

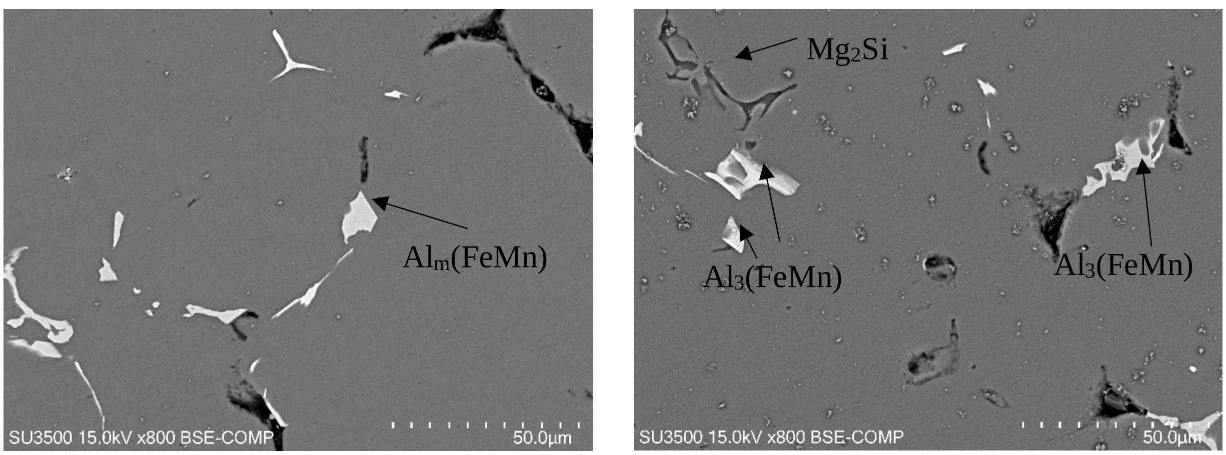

Figure 2.19 SEM & BSE analysis-Middle section

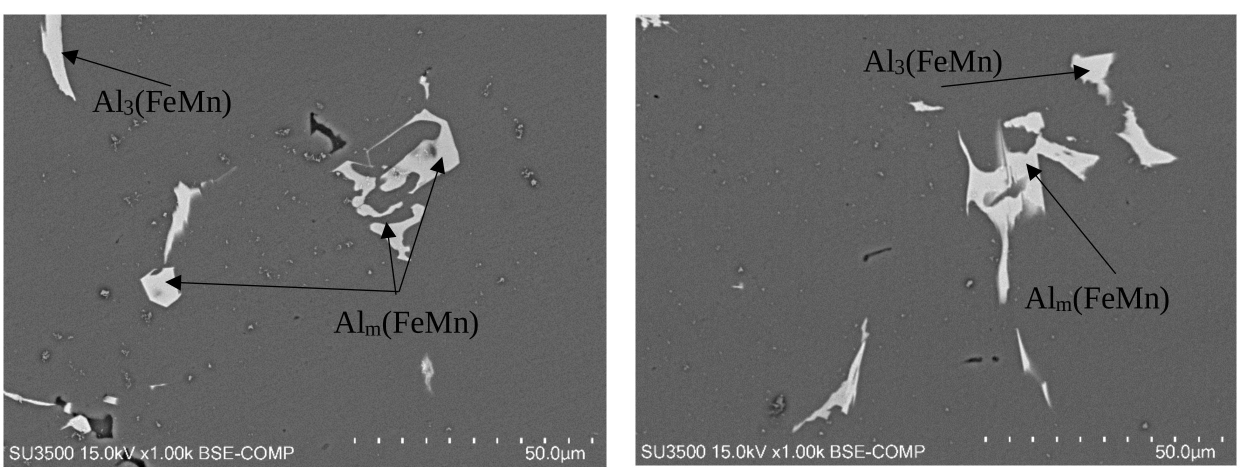

Figure 2.20 SEM & BSE analysis-Top section

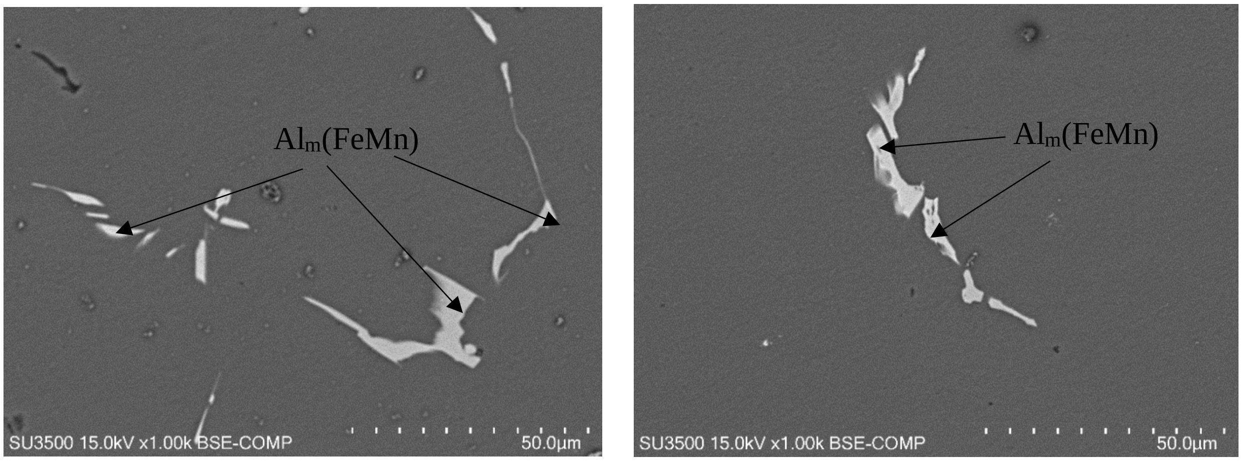

Figure 2.21 SEM & BSE analysis-Bottom section

Table 2-3 BSE composition analysis

(At%)	Al	Fe	Mn	Atomic Ratio Al/(Fe+Mn)	Particle Type
Middle	77.7	14.3	7	3.647	Al_3(FeMn)
	76.5	15.5	6.9	3.415	Al_3(FeMn)
	82.0	12.9	5.1	4.600	Al_m(FeMn)
	81.7	12.2	5.4	4.642	Al_m(FeMn)
	81.0	13.5	5.5	4.263	Al_m(FeMn)
	82.3	12.2	5.5	4.649	Al_m(FeMn)
Top	78.0	10.0	7.3	4.508	Al_m(FeMn)
	80.8	13.7	5.5	4.208	Al_m(FeMn)
	79.2	8.7	8.7	4.551	Al_m(FeMn)
	82.1	11.2	5.4	4.945	Al_m(FeMn)
	77.2	16.2	6	3.477	Al_3(FeMn)
	77.6	15.9	5.7	3.592	Al_3(FeMn)
Bottom	80.7	14	5.3	4.181	Al_m(FeMn)
	80.9	13	5.7	4.326	Al_m(FeMn)
	82.3	11.4	5.1	4.987	Al_m(FeMn)
	81.2	13.3	5.5	4.319	Al_m(FeMn)
	81.2	13.3	5.4	4.319	Al_m(FeMn)
	81.3	11.1	6.6	4.593	Al_m(FeMn)

2.5 Surface Quality

In order to get a better picture of the surface roughness, 3D Roughness Profilometry was performed on both, top, and bottom surfaces, of the as-cast AA5182 strips, with the domain of interest set to 3 mm by 3 mm. The results are shown below.

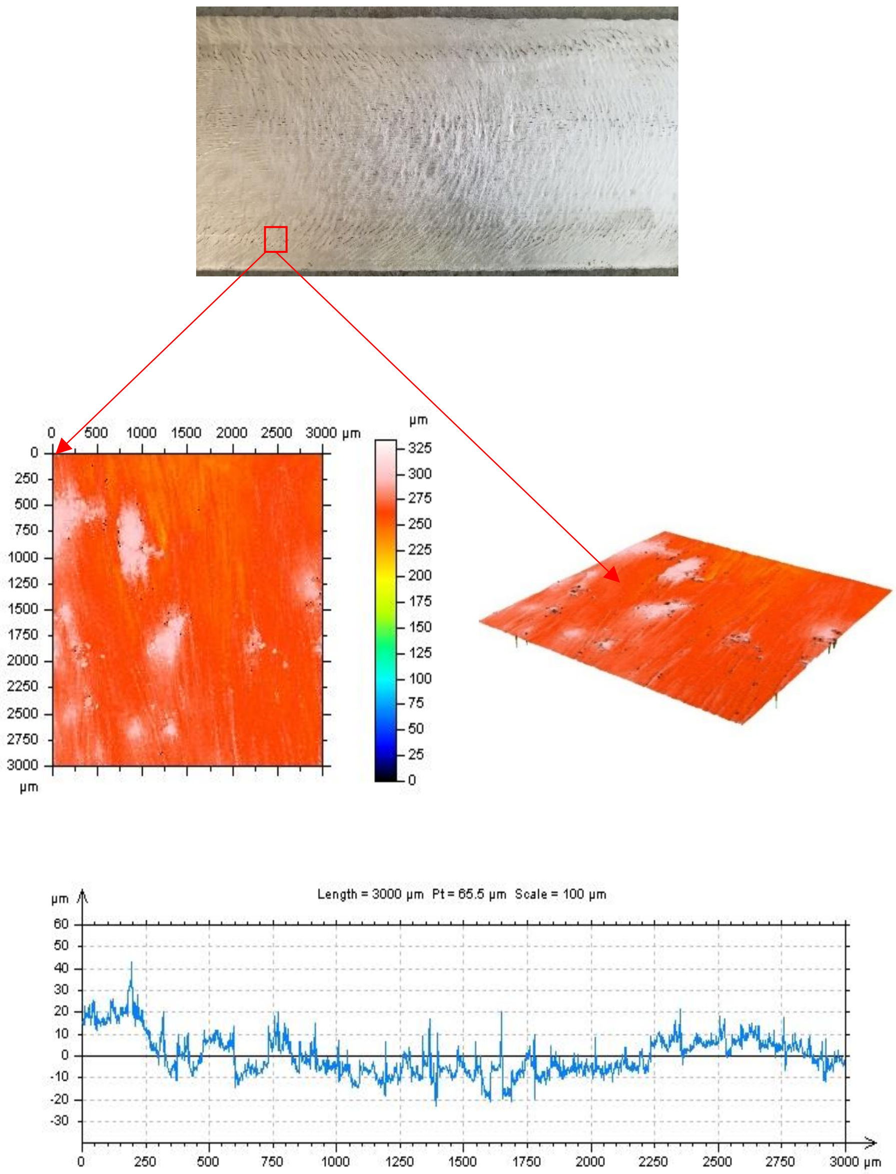

Figure 2.22 Bottom surface quality

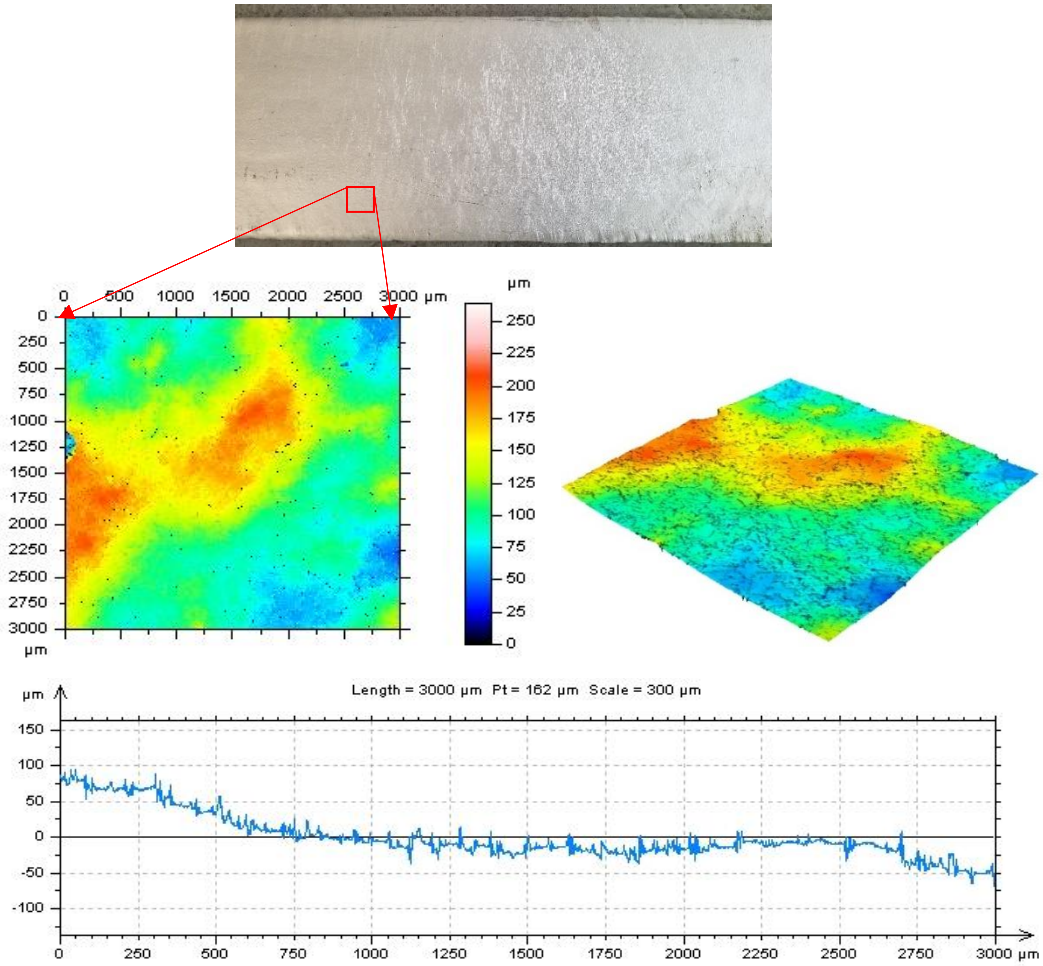

Figure 2.23 Top surface quality

Figure 2.22 shows the bottom surface of the strips. As can be seen, the height distribution is very uniform with slight deviations of $\pm 20\ \mu m$. On the other hand, the top surface (Figure 2.23) is rougher with its relative heights more widely distributed i.e. the top peak at 100 μm and lowest peak at -50 μm. This is as expected, since the HSBC process is an asymmetric solidification process. The top surface solidified in open air, at cooling rates lower than that which the bottom surface experienced. The nucleation sites, as well as the grains, are more uniformly packed due to high heat flux. As mentioned, for pilot scale casting experiments, a thin layer of graphite coating was applied on to the belt to promote better separation of the melt from the belt substrate.

2.6 Mechanical Properties

The hardness of the as-cast AA5182 HSBC strips were measured using the Vickers hardness test. In addition, the shear punch tests (SPT) were performed on a strip's sample grounded down to 0.67mm thickness. Due to the lack of material availability, the SPT is a good alternative technique that can be used to evaluate the mechanical properties of thin metallic sheet materials. Note that in order to convert the yield shear stress τ_{ys} and the ultimate shear stress τ_{uts} obtained from the SPT to tensile stress σ, the following relations were used.

$$\sigma_{ys} = 1.77\tau_{ys}\ , \sigma_{uts} = 1.8\tau_{uts}$$

The results were shown in the two tables below along with the stress-strain curves plotted using MATLAB.

Table 2-4 Vickers Hardness Measurements for AA5182 HSBC Strips

Typical Hardness Value for AA5182 (HV)	Bottom (HV)	Top (HV)2
84	98.01	87.64
	85.03	77.24
	80.49	80.49
	83.95	87.64
	89.58	95.76
	82.19	85.77
	85.77	85.03
	82.19	80.49
	Average	**Average**
	85.90 ± 5.26	85.00 + 5.37

Table 2-5 Shear Punch Test Results and Estimated Tensile Stresses

Average Yield Shear Stress (MPa)	Average Ultimate Shear Stress (MPa)	Average Yield Stress (MPa)	Average Ultimate Tensile Stress (MPa)
198 ± 13.44	216 ± 12.67	350.46	388.8

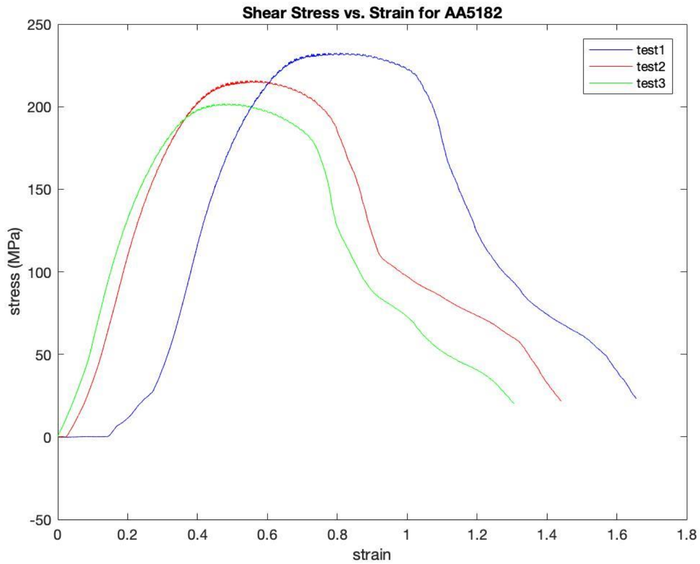

Figure 2.24 Stress-Strain Curves obtained from SPT

As can be seen from the hardness results, the as-cast AA5182 HSBC strips have relatively consistent hardness on the both sides with the bottom being slightly higher. Both values, however, are 1 HV higher than the conventionally processed AA5182. In terms of the yield and ultimate tensile stresses, the theoretical values are 130 MPa and 275 MPa respectively. It is clearly seen that the HSBC strip products have much higher strength compared to those produced with the traditional method. These significant improvements were able to be made simply due to the much smaller grain size that the HSBC process can achieve with its inherently high cooling capability.

3. Chapter 3 Fluid Flow Simulation of AA5182 Alloy-Computational Fluid Dynamics (CFD) Modeling

3.0. Introduction

Computational Fluid Dynamics (CFD) has been proved to be very useful in simulating metallurgical processes. Commercial codes and software have been invented to aid in these simulations. One of the most commonly used software is the ANSYS-FLUENT. It is a very powerful tool that can give close to reality physical prediction and description to fluid flow, heat and mass transfer. All governing equations, such as those for conservation of mass, momentum and energy equation were discretized and solved using the control volume formation, or what they called the Finite Volume Method (FVM) in the ANSYS-FLUENT.

3.1 Numerical Simulation Models

The transient state flow field and thermal behavior of a proposed liquid metal delivery system and the belt region next to it, was simulated using the commercial software ANSYS FLUENT 14.5. The simulation domain was constructed and meshed as shown in Figure 3.1.

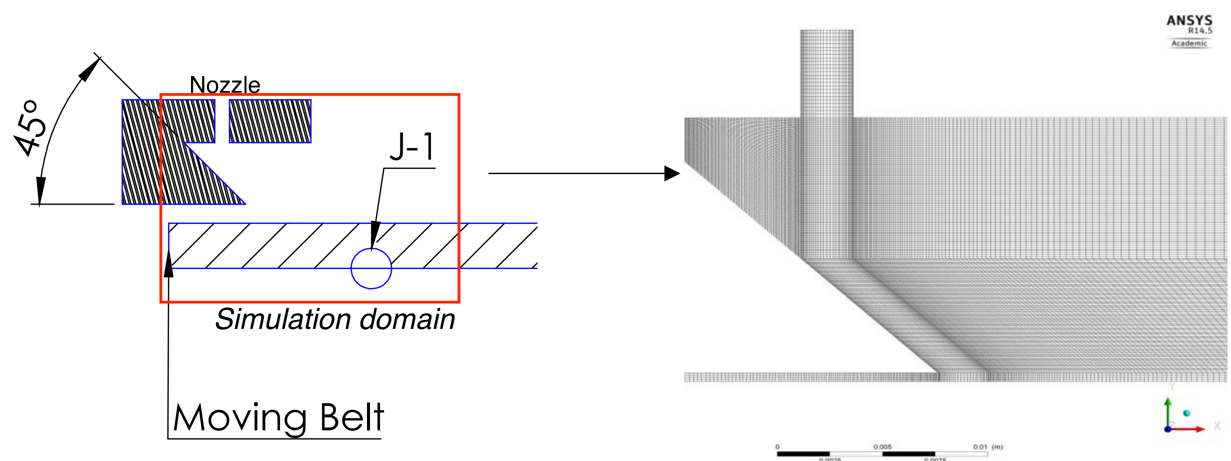

Figure 3.1 Simulation domain and meshing

The inclined plate was at 45 degrees to the horizontal axis, with the nozzle exit above it, aiming at its mid-point. The simulation domain was meshed into a 3.4 x 10^4 structured grid assembly, having variable mesh sizes ranging from 3.1 x 10^{-5} to 9.9 x 10^{-4}m.

The governing equations, such as those for conservation of mass and momentum, as well as the energy equation, were solved using the Finite Volume Method (FVM). The pressure-based solver applied for this simulation assumed that the melt was an incompressible Newtonian fluid. In order to better capture the interface between the air and the melt (two immiscible phase fluid flow), the Volume of Fluid (VOF) model was adopted, so as to track the transient locations of the upper free surface.[41] Since the model accounts for a mixture of multiple fluids, the simplest assumption (based on simple fluid and gas mixture laws) can be made as followes:

$$\rho = \sum \rho_k C_k \tag{25}$$

$$\mu = \sum \mu_k C_k \tag{26}$$

where ρ is the mixture density, comprising the density of molten AA5182 and air, and μ is the averaged turbulent viscosity. The subscript k refers to fluid k and C_k is the k-th fluid volume fraction. This can be defined as follows:

$$\mathrm{C_k} = \frac{V_k}{V} \tag{27}$$

with V_k being the volume of k-th fluid within a control volume V. Although it is assumed the system is filled with incompressible fluid, that is, ρ is constant, ρ_k is not necessarily the same as it may change over time within an element. The transient state model helps keep track of the change of each fluid density, in each control volume element. With these factors in mind, the governing continuity and conservation of momentum equations for VOF model can be expressed as follows:

$$\sum\left[C_k\left(\partial_t\rho_k + \bar{V}_j\partial_j\rho_k\right) + \rho_k\left(\partial_t C_k + \bar{V}_j\partial_j C_k\right)\right] = 0 \tag{28}$$

$$\sum C_k[\partial_t(\rho_k\,\bar{V}_i) + \partial j(\rho_k\bar{V}_j\bar{V}_i) - \partial_j(\mu(\partial_j\bar{V}_i + \partial_i\bar{V}_j))] = -\sum\partial_i(C_k p) + \sum \mathrm{T}_{ij}^k\partial_j C_k \tag{29}$$

Since the two fluids (melt and air) are assumed not to diffuse or to react with each other (a simplification), the term $\partial_t C_k + V_j\partial_j C_k$ in the continuity equation 28, can be set to zero. In terms of the conservation of momentum (eq. 29), it is assumed that the fluid is an ideal mixture. As such, $P = \sum P_k$, where $P_k = C_k P$ is the partial pressure for the k-th fluid. Note that all the above terms are expressed in terms of time-averaged values for the Reynold Averaged Navier Stokes (RANS) equations are used. The term labelled in red, $\rho_k\bar{V}_j\bar{V}_i$, is the Reynold stress tensor which requires closure to solve for the values. For this, the two equations $k-\omega$ SST (Shear Stress Transport) turbulent model was employed to solve the value and to capture the turbulent behavior of the flow. [42] The basis of this two-equation model is the Boussinesq eddy viscosity assumption, that assumes the stress term T_{ij} is proportional to the mean strain rate tensor as shown in the equation below.

$$-\rho_k\bar{V}_j\bar{V}_i = T_{ij} = 2\mu_t S_{ij} - \frac{2}{3}\rho k\delta_{ij} \tag{30}$$

where μ_t is the eddy viscosity which is calculated from the two transported variables, that is, k the turbulent kinetic energy, and ω, the specific turbulence dissipation rate. The two variables introduce two extra transport equations to account for the convection and diffusion of turbulent energy. The equations for the turbulent kinetic energy (eq.31) and specific dissipation rate (eq.32) are shown as follows;

$$\partial_t k + U_j \partial_j k = P_k - \beta k\omega + \partial_j[(\nu + \sigma_k \nu_T)\partial_j k] \tag{31}$$

$$\partial_t \omega + U_j \partial_j \omega = \alpha S^2 - \beta \omega^2 + \partial_j\left[(\nu + \sigma_\omega \nu_T)\partial_j \omega\right] + 2(1 - F_1)\sigma_{\omega^2} \frac{1}{\omega}\, \partial_i k \partial_i \omega \tag{32}$$

All of the closure coefficients and auxiliary relations for these two equations can be found in the conference proceedings paper by Menter, F.R. (1993). The reason the $k - \omega$ SST model was chosen for this simulation was due to its convenience in switching between $k - \omega$ and $k - \epsilon$ in facing different flow regimes. At the inner boundary layer region, all the way to the contacting wall, the $k - \omega$ formulation is applied to compute the low-Re turbulence phenomenon. Similarly, at the free stream region, this SST model allows the turbulence model to change into the $k - \epsilon$ formulation, so as to avoid any high sensitivity to the guessed value of the inlet free stream turbulence.

To model the thermal behavior and temperature distribution, the energy model was switched on. The governing equation used is the conservation of energy with time-averaged expression, shown as follows;

$$\partial_t \overline{T} + \overline{U_i} \partial_i \overline{T} = \alpha \partial_i \partial_i \overline{T} - \partial_i \overline{T\, U_i'} \tag{33}$$

The results obtained from the energy equation was later used for solidification model. Finally, the PISO algorithm was employed to deal with the transient state pressure-velocity coupling. For convenience, the power law scheme was used for the momentum equations, in order to account for all Peclet number situations.

3.2 Simulation Details

Boundary Conditions and Casting Parameters:

1. At the inlet, the velocity magnitude was set to 0.8 m/s normal to the boundary, so as to give the initial melt flow entering from the nozzle. The temperature of the melt was set to $940^{o}K$.
2. As for the open-air boundary, the pressure-outlet was selected with 0-gauge pressure i.e. at the same pressure as the operating condition, at the atmospheric pressure. The temperature was set to be $300^{o}K$. Same conditions are applied to the meniscus region located at the gap region between the bottom tip of the ramp and the moving belt.
3. The horizontal belt was set to be a non-slip moving wall boundary moving at 0.4 m/s. The contact angle between the melt and the steel belt was 120 deg, and 125 deg for the contact angle between the melt and refractory walls. The belt was given a constant temperature condition of $300^{o}K$.
4. For all other wall boundaries, stationary-no slip boundary conditions were applied.

Table 3-1 AA5182 properties used in Fluent setup [43]

Density (kg/m^3)	2600
Cp, Specific Heat (j/kg-K)	904
Thermal Conductivity (w/m-K)	126
Viscosity (kg/m-s)	0.00129
Molecular Weight (kg/kgmol)	27
Standard State Enthalpy (j/kgmol)	1.100493×10^{7}

3.3 Results and Discussion

3.3.1 Fluid Flow Behaviors at First Impingement

It is of interest to investigate the flow behavior of the melt during its first impingement on the sloped ramp. Some results during the transient feeding of metal on to the ramp, are shown below. From Figure 3.2, it can be seen that at the earlier time-step (t=0.027s), the melt film shape is relatively irregular. Nevertheless, as time progresses from the “start cast”, it is seen that at a later time-step (t=0.030s), the melt film became more uniform in terms of thickness. As mentioned before, this is a desirable situation, as the ramp is designed to exert extra frictional forces in addition to that of gravity, in order to reorganize the flow field into one that is more stable when it touches the belt. At t=0.033s, a slight volume build-up at the front of the metal flow can be observed. This is possibly due to the higher traveling speed of the melt located at upper portion, as compared to the melt near the ramp where the no-slip condition that holds the liquid aluminum back. This provides us with a better insight on how to optimize the length of the ramp, in order to avoid such a phenomenon.

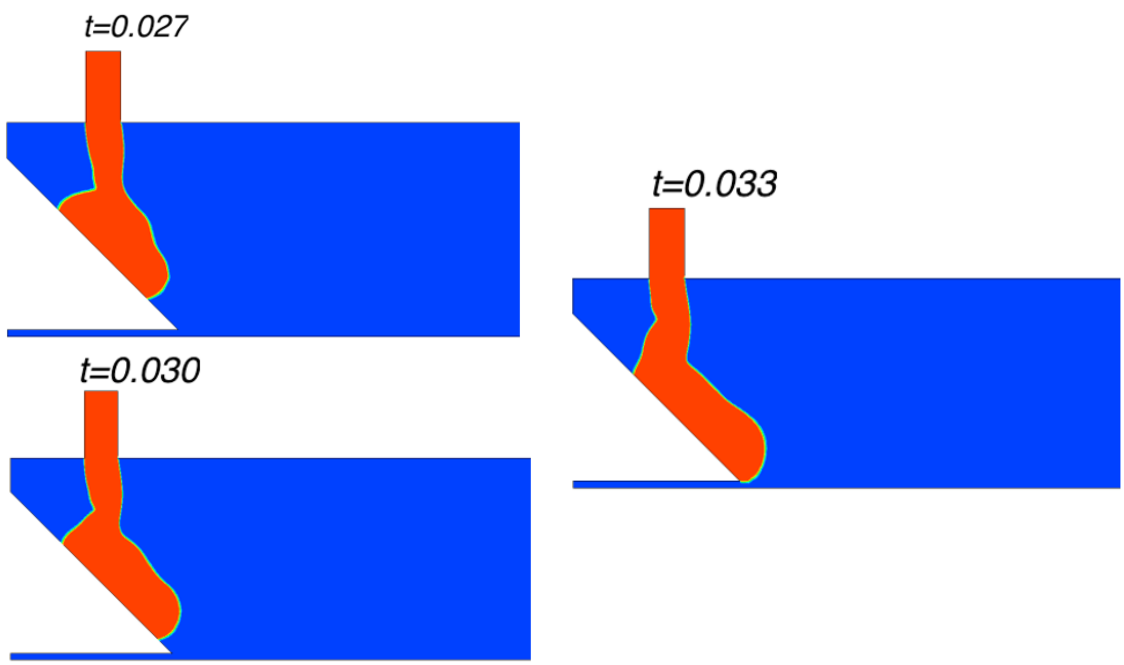

Figure 3.2 Effect of gravitational and frictional force on flow regeneration

In Figure 3.3, the first impingement area is enlarged to show a couple of details regarding the flow's behavior. It is clearly seen that at the impingement point, the flow is separated into an upward and a downward flow.

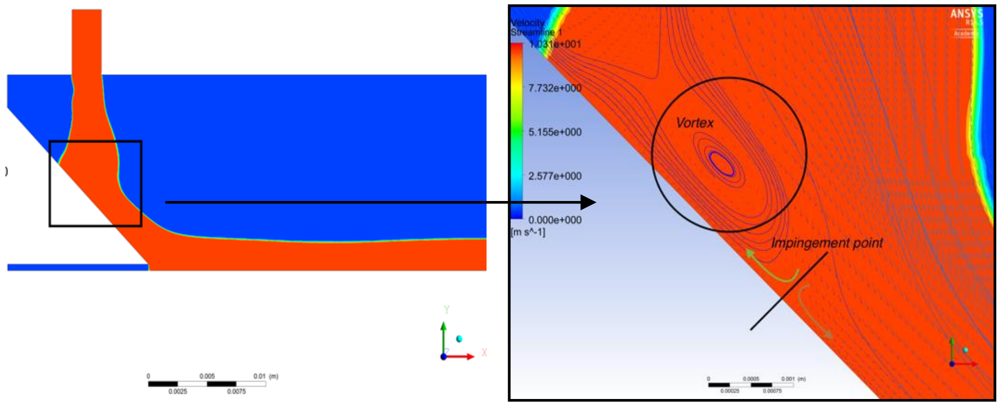

Figure 3.3 First impingement

The upward flow gives rise to the swirl-like flow field, generating a tiny vortex region close to the wall. The existence of this vortex could possibly cause the instability of the melt film and an air entrapment issue, generating central porosity.

3.3.2 Fluid Flow Behaviors at Second Impingement

Another interesting feature observed is the fluid flow behavior at the second impingement as shown in Figure 3.4. Looking at the far field velocity, that is away from the refractory wall, the flow is rather smooth compared to its upstream flow at the first impingement. The ideal of iso-kinetic condition, however, was not fully met as the velocity of the top surface was still higher than the belt's speed. The associated surface instability issue will be discussed later.

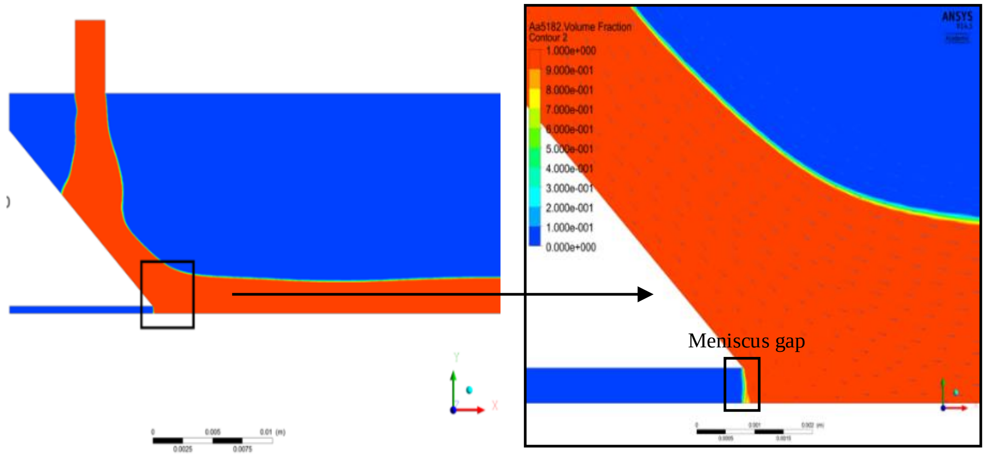

Figure 3.4 Second impingement

Another important feature worth mentioning is the meniscus behavior. Since the melt feeding process was transient, it is observed that at the meniscus gap region as indicated, the air-melt interface fluctuated slightly, and the melt penetrates backward a little passed the tip of the ramp. Below Figure. 3.5 shows one single cycle of the fluctuation behavior that potentially occur during the HSBC process. At t=0.82s, the melt-air interface was found to be at the maximum penetration distance. According to the velocity profile, the region appeared to be quite unsteady and slightly chaotic. This generated a small turbulent flow at this specific time frame. As the belt movement continued, the turbulent kinetic energy slowly dissipated as the flow reorganizes itself i.e. t=0.821s, matching up the speed of the belt. At t=0.822, 0.823 and 0.824, the turbulence energy started to escalate again as the incoming melt interacted strongly with the air that was being carried along by the motion of the belt, causing the region to be unstable. The melt-air interface then goes through the same cycle continuously. Note that the development of such turbulent flow region is completely independent of its upstream flow behavior. From the model, it is seen that the turbulent energy is quite small and almost insignificant on the top. The only problem with the current nozzle's configuration is the turbulence that is induced by the small penetrating flow that fluctuates and interacts with air periodically, due to the wetting surface and the motion of the belt. This slight disturbed flow can affect the bottom surface quality of the as-cast strip in ways such as mixing air flow or compromised surface smoothness. Nevertheless, based on the surface quality analysis previously discussed, results showed that even though there was slight unevenness at the bottom, the deviation is within acceptable range. The strips can still be very easily rolled after casting. Although, these turbulences were detected, the negative effect was very well contained with the current setup.

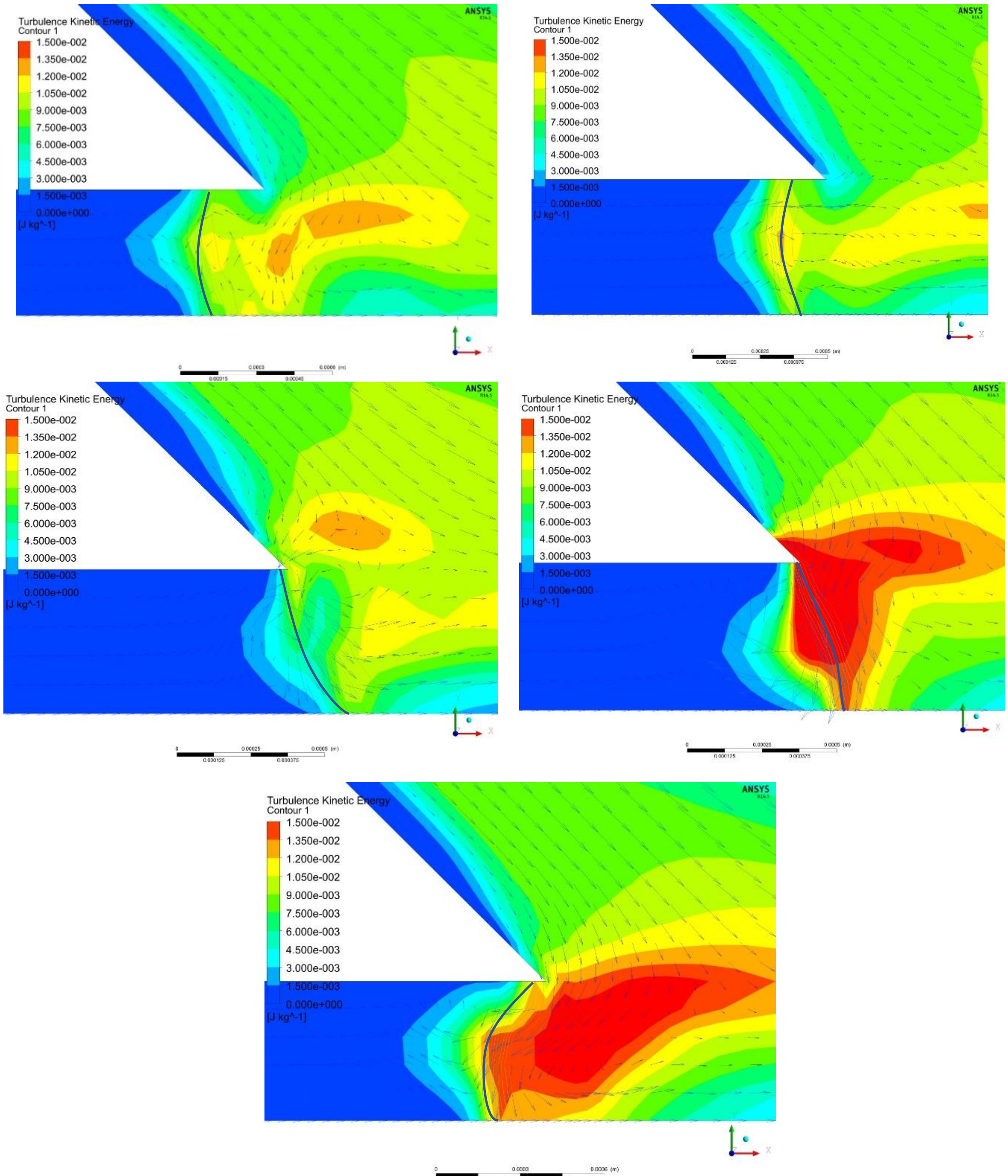

Figure 3.5 Turbulent kinetic energy at the second impingement at different time frame

3.3.3 Temperature Distribution and Solidification

Last but not least, in order to simulate the solidification process, it is first required to solve the energy governing equation. The simulated result is shown below in Figure 3.6. The region enclosed in the box gives a good overview of how the temperature is distributed. The water-cooled moving belt allows the bottom surface of the melt to be faster cooled down. At the region right adjacent to the second impingement, the dynamic pressure should be relatively high as compared to the outer horizontal region that is away from the back meniscus. Hence, the solidifying shell was expected to form further away down the stream as shown by Figure 3.6, the contour of liquid fraction. The blue region at the bottom represents the parts of the molten alloy that were completely solidified. The other colors in between the red and blue represent the mushy zone. As can be clearly seen, HSBC process features an asymmetric solidification mechanism with the melt solidifies in the direction from bottom to top. This type of solidification can greatly eliminate the problem of central segregation that is commonly found in the DC, TRC, and TBC processes.

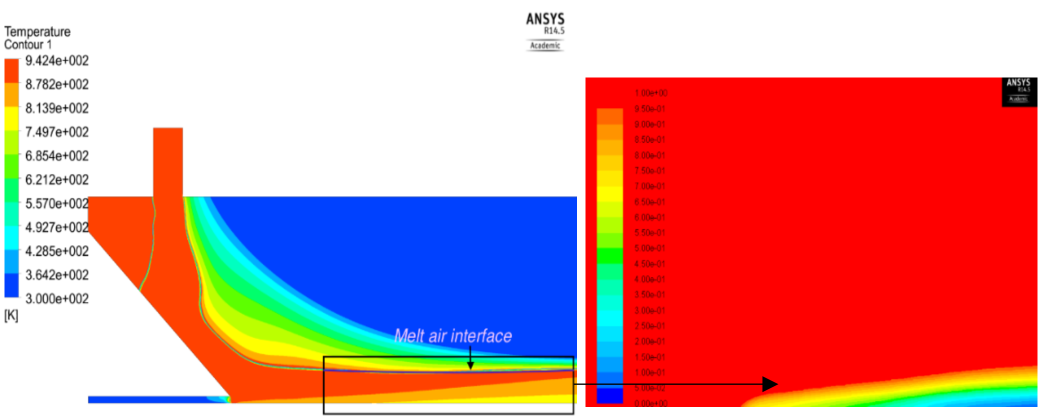

Figure 3.6 Predicted temperature distribution and solidification

3.3.4 Surface Instability

One important aspect worth studying is the surface instability that occurs during the casting process. As can be seen in Figure 3.2 shown previously, the top interface of the melt film featured a sinusoidal wavy contour as the liquid alloy fell freely by gravity down the inclined surface. It is found that in an open channel fluid flow system, the stability of the fluid depends greatly on the Froude number, or more specifically, the angle of inclination. As the angle increases, the stabilizing effect of gravity against the perturbating flow diminishes [44]. As discussed previously, perturbations can arise from the vortex structure located closed to the flow separation point, the frictional force the melt experienced as the melt travelled through the inclined ramp, and also the hydraulic jump phenomenon. It is estimated that the associate Froude number with the current HSBC setup is 5.5 with the assumed velocity being $0.8m/s$, the gravity acceleration $6.9m/s^2$, and the characteristic length being 3mm (opening width of the nozzle). The flow can therefore be considered as a supercritical flow, meaning that any sort of disturbances would be transmitted downstream [45]. In most cases, this early onset of laminar to turbulence transition states tend to amplify and evolve completely into a turbulent state [46]. Due to the different traveling speeds of the upper and the lower parts of the melt after the second impingement, this kind of disturbed flow field could easily turn into a larger vortex, causing the surface to roughen-up. According to the 3D profilometry analysis, the top surface of the as-cast AA5182 appears to be rather smooth, but a repetitive stripe pattern can be observed by eye. These stripes could possibly come from the solidified waves transmitted from the upstream. In order to prevent this, the velocity difference between the upper and lower part of the melt should be minimized. The relationship can be better understood by looking at the Kelvin-Helmholtz instability, as shown in Figure 3.7.

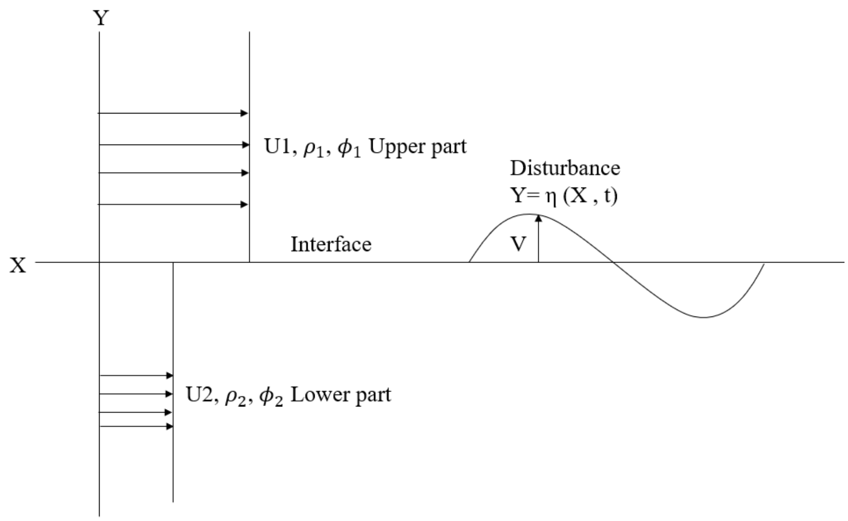

Figure 3.7 Discontinuous shear across an interface

The flow potential in this given area can be decomposed into the following.

$$\tilde{\phi} = \phi + \phi' \tag{34}$$

Where $\tilde{\phi}$ defines the disturbed velocity potential field, ϕ defines the base velocity potential field and ϕ' represents the perturbing velocity potentials. More specifically,

$$\nabla\tilde{\phi} = \begin{bmatrix} \tilde{u} \\ \tilde{v} \end{bmatrix} \tag{35}$$

$$\nabla\phi = \begin{bmatrix} U \\ 0 \end{bmatrix} \rightarrow base\ solution \tag{36}$$

$$\nabla\phi' = \nabla\tilde{\phi} - \nabla\phi = \begin{bmatrix} u' \\ v' \end{bmatrix} \rightarrow perturbation \tag{37}$$

In general, this instability is governed by the laws of incompressible and irrotational fluid flows. the interface kinematic condition and the unsteady Bernoulli equation deduced from Euler equation. The interface kinematic is required to set the condition that the interface between two fluids to move up and down with a velocity (V), equal to the vertical component of the fluid's velocity. In terms of the unsteady Bernoulli equations, it applies the condition that across the interface, the pressure is required to be continuous at any Y= η. Here Y= η (X, t) is used to describe interface that is deformed due to a perturbation. After applying both conditions mentioned to the defined perturbation equation (eq.37), the newly formed equations can be solved and described using the normal mode analysis. The normal mode analysis basically states that for an oscillating system, the pattern of movement will follow sinusoidal motion with all parts of the system having the same frequency. The general ansatz are shown as follows.

$$\eta = \hat{\eta} e^{ik(x-ct)} \tag{38}$$

$$\phi' = \hat{\phi}(y) e^{ik(x-ct)} \tag{39}$$

Here the k is a real number, and c is a complex wave speed that can be further broken down to this relationship $c = c_r + ic_I$. With this notation, the above two equations can be re-written as follows:

$$\eta = \hat{\eta} e^{ik(x-ct)} e^{C_I t} \tag{40}$$

$$\phi' = \hat{\phi}(y) e^{ik(x-c_R t)} e^{C_I t} \tag{41}$$

For physical interpretation, the two equations tell us that at a fixed point, the system is oscillating at a frequency equals to c_r, whereas the second part of the equation i.e. c_I determines the stability of this oscillation. For cases $c_I > 0$, the flow become unstable exponentially as time passes. Whereas for cases $c_I < 0$, the unstable waves die down exponentially. By solving above normal mode equations with all the boundary conditions described, the following solution is obtained [47-49].

$$c = c_r + ic_I = \frac{\rho_1 U_1 + \rho_2 U_2}{\rho_1 + \rho_2} \pm \left[\left(\frac{g}{k}\right) \frac{\rho_2 - \rho_1}{\rho_1 + \rho_2} - \rho_1 \rho_2 \left(\frac{U_1 - U_2}{\rho_1 + \rho_2}\right)^2 \right]^{\frac{1}{2}} \tag{42}$$

For the fluid to be stable, the part within the square root should have this relationship expressed as follows:

$$(U_1 - U_2)^2 < \frac{g(\rho_1^2 - \rho_2^2)}{k \rho_1 \rho_2} \tag{43}$$

With the fluid having approximately the same density i.e.$\rho_1 \approx \rho_2 \approx \rho$, the equation can be further simplified to [50]

$$(U_1 - U_2)^2 < \frac{2g(\rho_1 - \rho_2)}{k\rho} \tag{44}$$

Hence, it is clearly seen that by minimizing the velocity difference between the upper and lower parts of the melt right at the beginning can effectively eliminate such surface defects. Although with the current casting speed of 0.4 m/s, the critical velocity difference is not enough to cause the full onset of the instability, nonetheless, by limiting the velocity variation in the early stage can trigger the exponential decay to take place much earlier.

4. Chapter 4 Standard Melting & Subsequent Deformation for HSBC Aluminum Alloys Specimens- Hot Ductility Test

4.0 Introduction

Hot ductility mechanical tests were performed on the materials AA6111, AA5182 and AA2024 to investigate the deformation behavior of continuously cast aluminum alloys. The goal is to further study the suitable temperature for rolling following the HSBC process in order to avoid cracking of strip materials. All tests were carried out at Dynamic System Inc., USA, using a Gleeble machine 3500 series.

4.1 Sample preparation and Experimental Setup

Round bars were prepared from cast AA6111, AA5182 and AA2024 ingots. The dimensions of a bar specimen are shown in Figure 4.1 (as per standard). A total of three samples of AA6111 alloys, six samples of AA5182 alloy and four samples of AA2024 alloy were prepared.

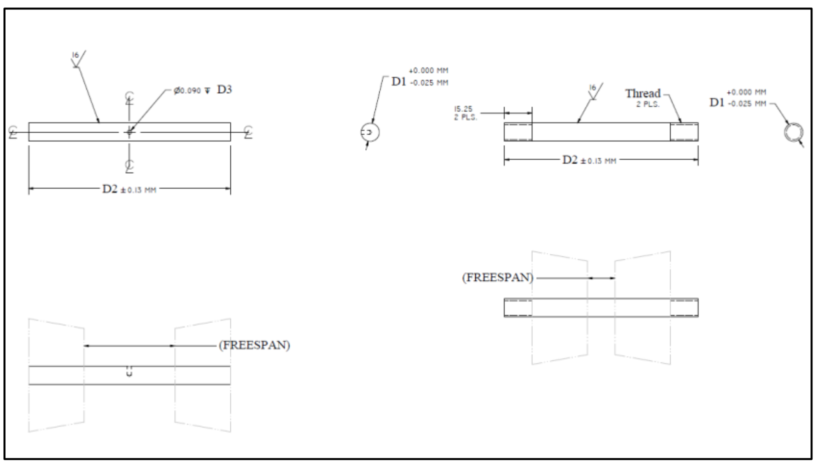

Figure 4.1 Bar specimen dimensions

4.1.1 K-type Thermocouple Attachment & Sample Set-up for Gleebel Test

A 0.040-inch diameter and 0.1-inch depth hole (Figure 4.2) were created by drilling through a machined sample in the middle, where melting and tensile pulling would take place. Thermocouple

(TC) was fit in the drilled hole with its surrounding aluminum alloy, mechanically hammered with pointed metal punch, in order to hold the TC wire in place (Figure 4.3). This method ensures very good thermal contact.

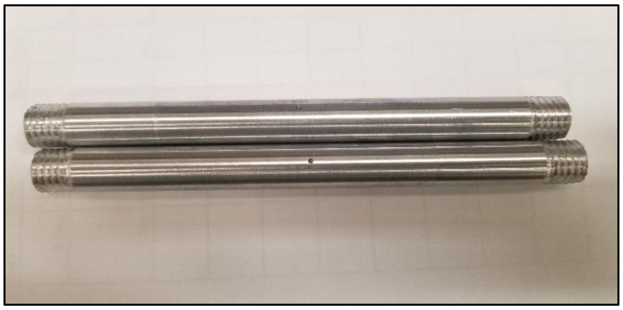

Figure 4.2 Drilled machined sample

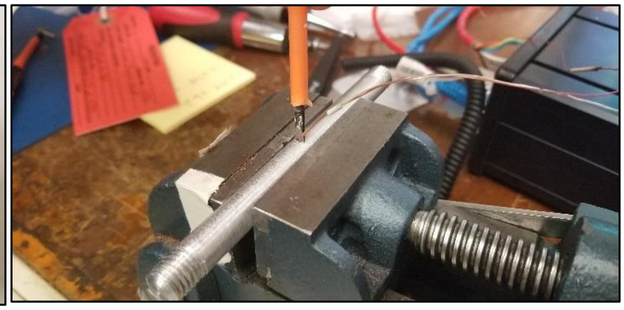

Figure 4.3 Thermocouple attachment method

Once the thermocouple was attached, a quartz crucible with a 10 mm inner diameter (ID), 30.5 mm in length, was placed right in the middle region of the sample, as shown in Figure 4.4. Each end segment of a sample was then fixed with a copper jaw holder (Figure 4.5). The two holders were then balanced to ensure zero net force acting on the specimen sample. The purpose was to isolate and expose the middle region to heating under tension. In addition, the copper material was used as a heat sink for efficient cooling.

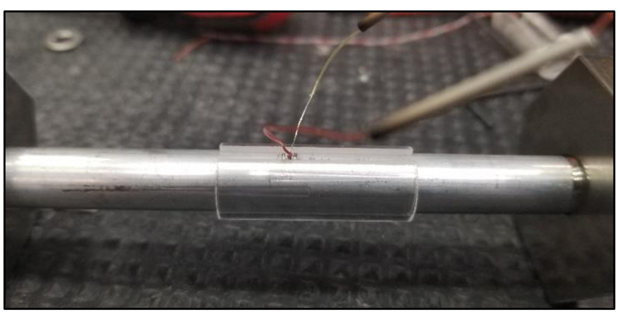

Figure 4.4 Quartz crucible placed in position

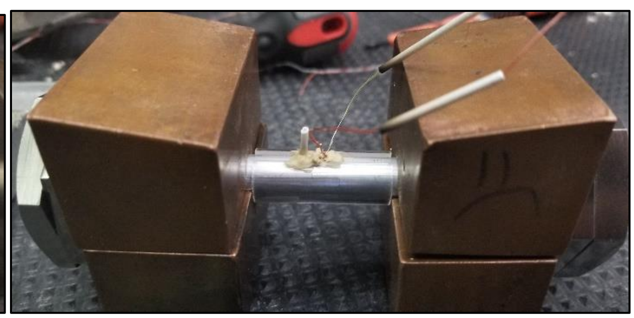

Figure 4.5 Copper jaw

Once ready, the whole sample, along with the copper jaws, were then transferred into the closed chamber of the Gleeble 3500 (Figure 4.6). The specimen was then levelled using the hydraulic and the AirRem systems of the machine. Forces are monitored throughout the adjustment to ensure zero net force on the sample (Figure 4.7). To simulate real time HSBC casting, followed by rolling, the whole experiment was performed under atmospheric conditions.

Figure 4.6 Gleeble 3500

Figure 4.7 Overall setup

4.1.2 Hot Ductility Program Setup

The tested specimen was first heated up to 525°C in 10.5s (i.e. 50°C/s heating) in the **Force (kgf)** mode. Force was set to zero to allow the mobile stroke to freely adjust itself, to ensure the net force stayed zero during the thermal expansion of the alloy. The system then was switched to **Stroke (mm)** mode. While the specimen was continuously being heated to 600°C, the distance between the stroke was fixed. Once the designated temperature was reached (i.e. 600°C), a "while loop" was executed to ramp up the temperature 0.5°C/s. In the meanwhile, a compression force was applied by shortening the stroke distance by 0.003mm every 2 second, in order to account for change in the material's volume during melting. The goal was to heat up the specimen close to its melting point, and then trigger the cooling immediately, so as to cool down to the tested temperature at a cooling rate of 100°C/s. The specimen was left at this temperature for 5 second to ensure complete stabilization (temperature uniformity). During this period, the distance between the stroke was set to zero as a reference point for the strain calculation. After this short delay in time, the tensile force was next applied at a rate of 0.001mm/s until fracture. Figure 4.8 shows a thermomechanical schedule of the hot ductility tests, and Figure 4.9 shows the worksheet of all pre-selected instructions and parameters to achieve the stress vs. strain curves. The detailed information about how the worksheet operate is explained in the flow chart below.

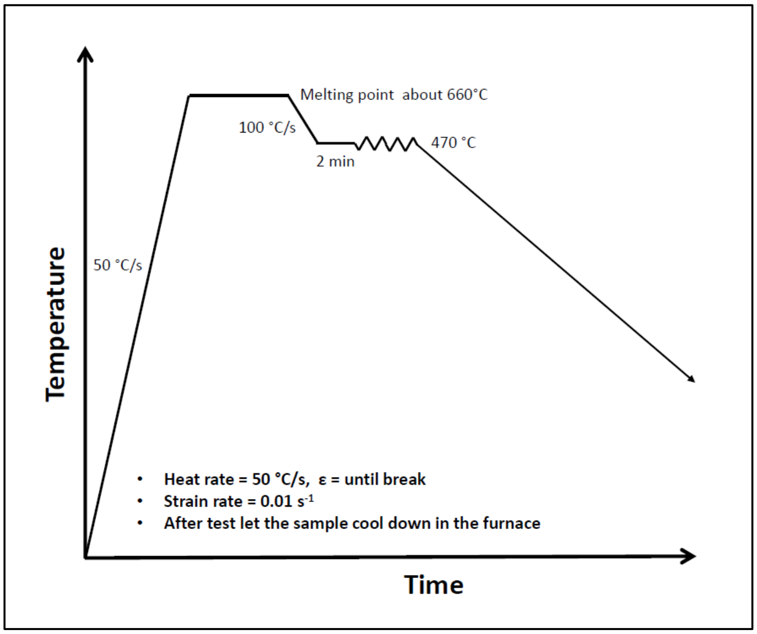

Figure 4.8 Schematic diagram of heating, cooling and strain rate parameters

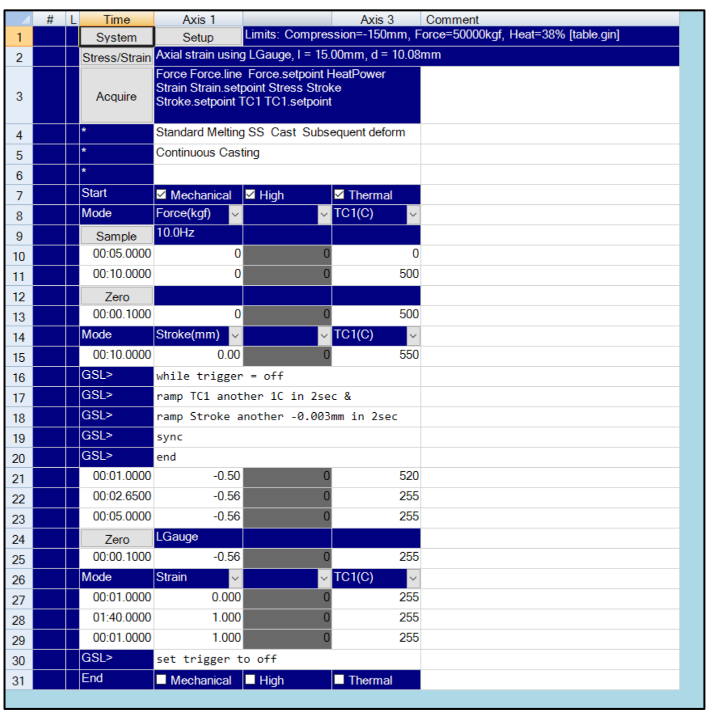

Figure 4.9 Worksheet for machine setup (written in C software)

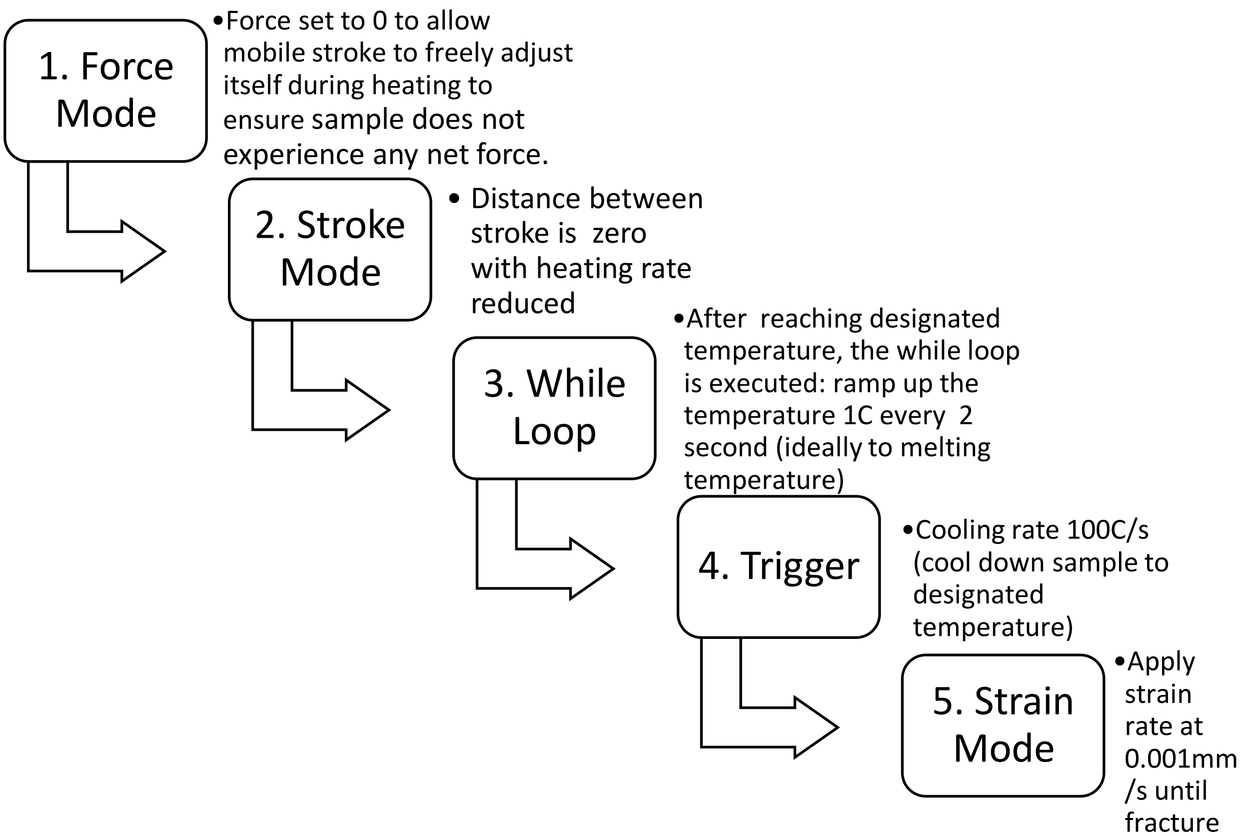

<u>Specimens, Targeted Melting Temperature & Temperature at Tensile Pulling</u>

Table 4-1 Testing parameters

	AA5182		**AA6111**		**AA2024**	
Trial	*Melting T(°C)*	*Tensile T(°C)*	*Melting T(°C)*	*Tensile T(°C)*	*Melting T(°C)*	*Tensile T(°C)*
1	620	478	630	470	570	383
2	615	478	610	470	550	255
3	610	478	600	255		
4	605	383				
5	605	319				
6	605	255				

4.2 Results & Discussions

Due to experimental limitations, the maximum temperature reachable without causing the tested sample to explode was 630°C. This temperature was then selected to be the target melting temperature for AA6111. During the first test with the AA6111 alloy, the sample broke into half at 580°C during heating. Neither cooling nor tensile pulling were performed, hence not enough data were obtained to construct stress vs. strain curve. This situation happened also to the first and second tests of the AA5182 alloy and second test of the AA2024 alloy. For all these samples, the cross section at the fracture interface all possess clear melt structure as can be seen in Figure 4.10 & 4.11.

Figure 4.10 Material failure before cooling and tensile pulling

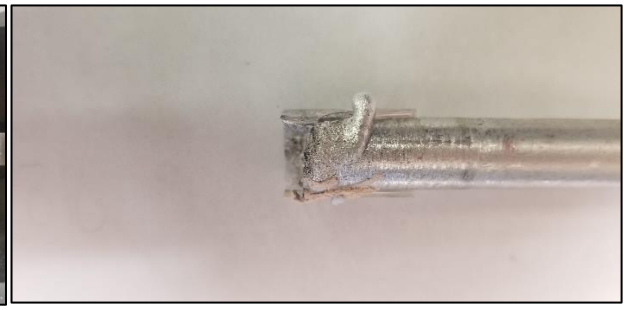

Figure 4.11 Failed specimen

The possible reasons for these failures are now discussed and elaborated as follows. The first possible cause was that the thermocouple attached to the sample might have experienced slight displacement, and that caused the computer to pick up lower temperature readings than the material's actual temperature. The computer responded to this situation by increasing the amount of current and eventually, caused the sample to overheat and fracture. Another reason was that the quartz crucible used did not provide adequate room for the tested sample to thermally expand during heating. Hence, the crucible broke half way and provided no support to the sample. In order to avoid this, the dimensions of the crucible and the machined samples will need to be adjusted. For future hot ductility tests, a bar specimen with 6mm diameter is proposed.

Despite of all the difficulties, three test results did come out successfully i.e. test #3, 4 and 5 for the AA5182 alloy. In the case of test #3, successful heating and cooling were achieved, and that was followed by straining the sample at a rate of 0.01mm/s. This sample, however, experienced sudden fracture 3 seconds after the pulling. The cross section appeared to be similar to that of the

HSBC as-cast strip when rolling was applied (Figures 4.12 & 4.13). In the case of test # 4 and 5, tensile testing was successfully conducted. During pulling, necking behavior of the specimen was observed (Figure 4.14).

Figure 4.12 Brittle fracture surface (478C)

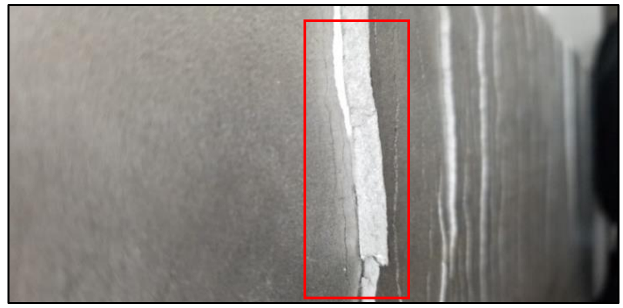

Figure 4.13 Brittle fracture surface of HSBC strip

Figure 4.14 Necking (383C)

In terms of the stress-strain curves for AA5182 tests # 4 and # 5, they are shown as followes in Figure 4.15 and 4.16, respectively. One curve for the alloy AA2024 is presented in Figure 4.17. As can be seen, the yield strength for the AA5182 at 383°C (Figure 4.15) was 70.3 MPa and failure strain 0.13. On the other hand, at 319°C (Figure 4.16), these values have been 114 MPa and 0.16, respectively. For the AA2024 at 383°C (Figure 4.17), the value of the stress was 70.3 MPa (same of the AA5182), but the strain was much lower, 0.01. The AA5182 samples exhibited an elastic behavior on the first part of the curves. After their yield stresses, they presented work hardening mechanism until reaching their maximum load. After this stage, the softening mechanism started to operate until the samples fractured. It is worth mentioning that the tested temperature represented 60% (383ºC) and 50% (319ºC) of the AA5182 melting point (T_m). For the AA2024 specimen, only the elastic regime was observed. The calculated toughness (area under the stress-strain curves) were 8.6 and 14.64 $J.m^{-3}$ for the 383ºC, and 319ºC tested samples, respectively.

It was attempted to apply deformation at 255ºC (40% T_m) to compare the result with 60%T_m and 50%T_m, however, all samples fractured during heating.

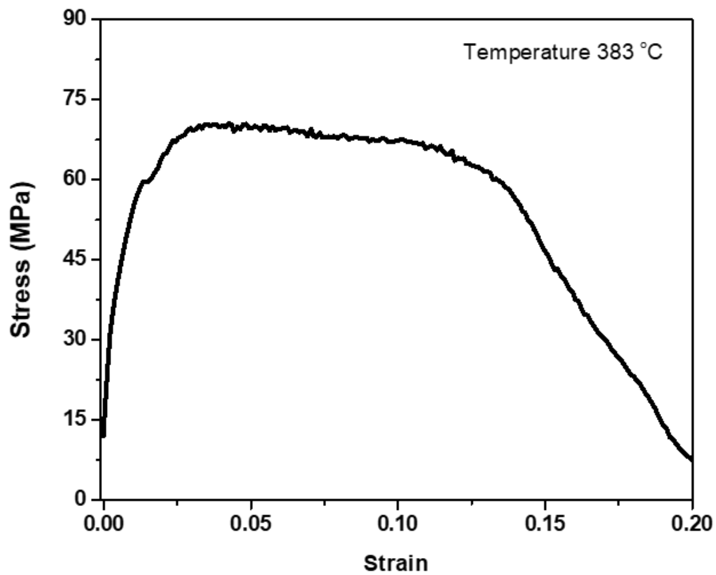

Figure 4.15 Stress vs strain of the AA5182 at 383 C

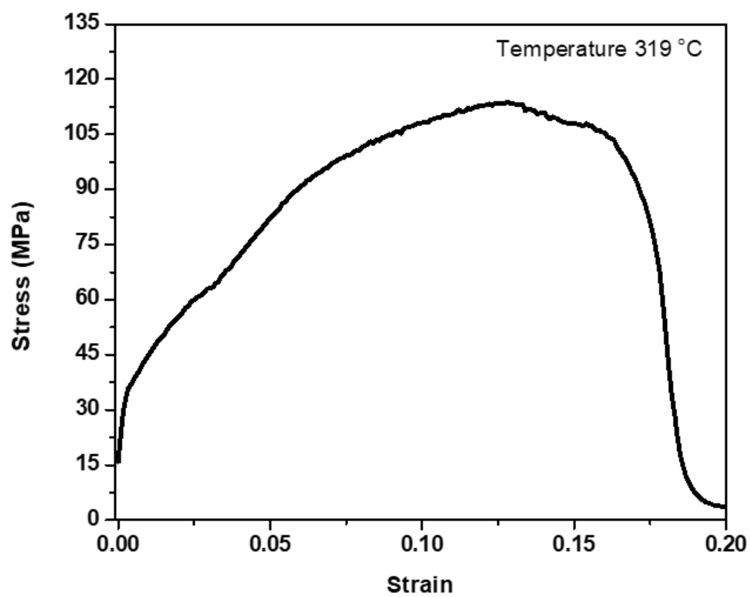

Figure 4.16 Stress vs strain of the AA5182 at 319 C

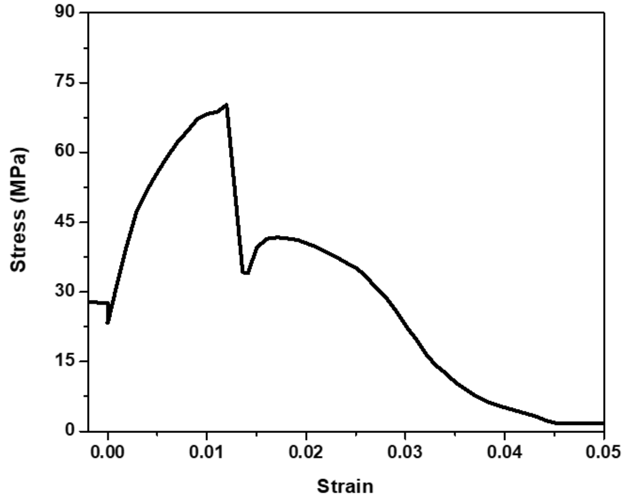

Figure 4.17 Stress vs strain of the AA2124 at 383 C

4.3 Conclusions

From the results obtained up to this point, it is concluded that during the cooling/solidification process, the material exhibits almost zero ductile behavior until the temperature reaches the temperature below roughly 470°C. The ductile behavior then slowly dominates, as temperatures keep dropping. According to the results presented, it is recommended that rolling should be applied only in the temperature range of 300-390, in order to avoid cracking. For future tests, revision of sample dimensions is necessary, and it is of interest to apply tensile deformations at much lower temperature i.e. 40% T_m.

5. Chapter 5 Conclusions

From the present study, the following conclusions can be drawn.

1) 200 and 250mm wide AA5182 thin strips with consistent thickness of 5mm were successfully produced via the MMPC-HSBC processing method.
2) Normal levels of porosity are observed in the as-cast strip products. Bulk porosity within the top and bottom regions are a little less compared to the central region of the strips, possibly due to slight variations in heat flux. In terms of the porosity level at the top and bottom surface, the number is close to none. This should make future post-casting processing steps to be easier.
3) When comparing the porosity level between the two different alloys, AA5182 and AA2024, the former was found to have slightly higher number of pores. It was found that that cause is not due to the HSBC process, but the wt.% Mg contents present in the alloys. It had been proven that with increased wt.% Mg, the solubility of hydrogen also increases, causing pore formation.
4) Owing to the inherent efficient cooling mechanism of the HSBC process, the average grain size of the as-cast AA5182 strips was found to be 63.1 µm, much smaller compared to those found in DC casting samples i.e. 123 µm. In terms of the secondary phase particles presented, the majority are found to be in the preferred phase $Al_m(Fe,Mn)$, which has a strong effect in enhancing the mechanical strength of the AA5182 material.
5) The as-cast AA5182 HSBC strips have very consistent hardness on the both sides and significantly stronger strength as compared to the conventionally processed AA5182 material.
6) Based on the CFD simulations, a vortex-like flow field was observed at the location close to the first impingement point where the flow separates. This structure as well as the supercritical

flow can lead to slight surface perturbations. Learning from the conditions for instability formation, it is suggested that in order to eliminate the unstable waves that solidified on the top surface, the velocity difference between the top and bottom portion of the melt should be limited.

7) Turbulent flow was found at the meniscus gap region. The cause of formation is due to the movement of the belt that drags in air to collide head on with the incoming melt. However, with the current belt travel speed, the turbulent air flow has very little effect in affecting the bottom surface quality, as shown by the 3D profilometry analysis.

8) Rolling should be applied at temperature lower than 0.6Tm (melting point) to prevent brittle fracture and to achieve efficient size reduction.

References

1. Maleki, A., A. Taherizadeh, and N. Hosseini, *Twin Roll Casting of Steels: An Overview.* ISIJ International, 2017. **57**(1): p. 1-14.
2. Barekar, N.S. and B.K. Dhindaw, *Twin-Roll Casting of Aluminum Alloys – An Overview.* Materials and Manufacturing Processes, 2014. **29**(6): p. 651-661.
3. T. Haga, H.S., H. Watari, and S. Kumai,, *High speed twin roll casting of 6061 alloy strips.* Archives of Materials Science and Engineering, 2008. **3**: p. 49–52.
4. H. Sakaguchi, T.H., H. Watari, and S. Kumai, *High speed twin roll casting of 6016 aluminum alloy strip.* Jouranl of Achievements in Materials And Manufacturing Engineering, 2007. **20**: p. 495-498.
5. Haga, T., et al., *A vertical-type twin roll caster for aluminum alloy strips.* Journal of Materials Processing Technology, 2003. **140**(1-3): p. 610-615.
6. Haga, T., *Twin roll casting of aluminum alloy strips.*
7. Sahoo, S., *Review on Vertical Twin-Roll Strip Casting: A Key Technology for Quality Strips.* Journal of Metallurgy, 2016. **2016**: p. 1-13.
8. *EMC '91 Non-Ferrous Metallurgy - Present and Future.* Elsevier Applied Science.
9. Robert E. Sanders, J., *Technology Innovation in Aluminum Products.* Wrought and Sheet, 2001.
10. Akira Goto, H.N., Pizhi Zhao,Toshiya Anami *Aluminum sheet material technology supportint car.* 2011.
11. *United States Patnet Twin-Belt Continuous Casting Method Providing Control of the Temperature Operating Conditions at the Casting Belts.* 1976.
12. *United States Patent Method and Apparatus for Twin Belt Casting of Strip.* 1996.

13. P.Z. Zhao, T.A., I.Okamoto, K.Mizushima,K.M.Gatenby, M.Gallerneault, S.Barker K.Yasunaga, A.Goto, H.Kazama, N.Hayashi, *development of twin belt cast AA5000.* 2009.

14. Ge, S., M. Isac, and R.I.L. Guthrie, *Progress of Strip Casting Technology for Steel; Historical Developments.* ISIJ International, 2012. **52**(12): p. 2109-2122.

15. Ge, S., *Numerical and physical modeling of the horizontal single belt casting HSBC process.* 2015.

16. Ge, S., M. Isac, and R.I.L. Guthrie, *Progress in Strip Casting Technologies for Steel; Technical Developments.* ISIJ International, 2013. **53**(5): p. 729-742.

17. M. Schäperkötter, H.E., J. Kroos, M. Niemeyer, R. Schmidt-Jürgensen,, *Direct strip casting (DSC) An option for the production of HSD steel grades.*

18. Mert Celikin, D.L., Luis Calzado, Mihaiela Isac, Roderick I.L. Guthrie, *Horizontal Single Belt Strip Casting (HSBC) of Al-Mg-Sc-Zr Alloys*, in *TMS (The Minerals, Metals & Materials Society*. 2013.

19. Hirsch, J., *Aluminium Alloys for Automotive Application.* Materials Science Forum, 1997. **242**: p. 33-50.

20. Ferry, M., *Metallurgy of Alloys Suitable for Direct Strip Casting.* 2006: p. 1-24.

21. Morrison, G.k., *The Effect Of Stabilization Heat Treatment On AA5182 Aluminium Alloy*, in *Mechanical Engineering*. 2013, University of Cape Town.

22. Hollomon, J.H., *Tensile deformation.* Trans. AIME, 1945. **162**: p. 268-290.

23. Y.J. Li, L.A., *Solidification structures and phase selection of iron-bearing eutectic particles in a DC-cast AA5182 alloy.* Acta Materialia, 2004. **52**(9): p. 2674-2681.

24. Thompson, S., *Effect of Cooling rate on Solidification Characteristics of ALuminum Alloys A356 and AA5182*, in *Metals and Materials Engineering*. 2003, University of British Columbia.

25. Yulin Liu, G.H., Yimeng Sun, Li Zhang, Zhenwei Huang, Jijie Wang, Chunzhong Liu, *Effect of Mn and Fe on the Formation of Fe- and Mn-Rich Intermetallics in Al–5Mg–Mn Alloys Solidified Under Near-Rapid Cooling*. 2016.

26. Patankar, S.V., *Numerical heat transfer and fluid flow*. Series in computational methods in mechanics and thermal sciences. 1980, Washington New York: Hemisphere Pub. Corp. ; McGraw-Hill. xiii, 197 p.

27. Spalding, D.B. and S.V. Patankar, *Numerical prediction of flow, heat transfer, turbulence, and combustion : selected works of Professor D. Brian Spalding*. 1983, Oxford ; New York: Pergamon Press. 430 p.

28. Patankar, S.V. and D.B. Spalding, *Heat and mass transfer in boundary layers : a general calculation procedure*. 2nd ed. 1970, London: Intertext. ix, 230 p.

29. ntut, *Finite-Volume (control-Volume) Method-Introduction*.

30. Thomas, L.H., *Elliptic Problems in Linear Differential Equations over a Network*. 1949, Columbia University.

31. Strong, D.M., *Iterative Methods for Solving Ax = b - Gauss-Seidel Method*. MMA Press.

32. Scarborough, J.B., *Numerical Mathematical Analysis*. 1955, Johns Hopkins Press.

33. Kopeliovich, D., *Degassing treatment of molten aluminum alloys*.

34. Xiaoming Wang, Q.H., *Grain Refinement Mechanism of Aluminum by Al-Ti-B Master Alloys*, in *TMS (The Mineral, Metals & Materials Society)*. 2016.

35. Ulanovskiy, I.B., *Hydrogen Diffusion and Porosity Formation in Aluminum* 2015.

36. P.D.Lee, R.C.A., R.J. Dashwood, H.Nagaumi, *Modeling of porosity formation in direct chill cast aluminum-magnesium alloys.* Materials Science and Engineering: A, 2002. **328**(1-2): p. 213-222.

37. Nagaumi, H., *Prediction of porosity contents and exmaination of porosity formation in Al-4.4%Mg DC slab.* Science and Technology of Advanced Materials 2, 2001: p. 49-57.

38. Hiromi Nagaumi, K.T., *Effects of Mg contents on porosity formation in Al-Mg alloy DC slabs.* Japan Institute of Light Metals, 2002. **52**: p. 293-297.

39. N. Jamaly, N.H., A.B. Phillion, *Microstructure, Macrosegregation, and Thermal Analyis of Direct Chill Cast AA5182 Aluminum Alloy.* ASM International, 2015.

40. Donghui Li, S.G.S., Mihaiela Isac, Roderick I.L. Guthrie, *Studies in the casting of AA6111 strip on a horizontal, single belt, strip casting simulator.* TMS, 2006.

41. Nichols, C.W.H.a.B.D., *Volume of Fluid (VOF) Method for the Dynamics of Free Boundaries.* Journal of Computational Physics, 1981. **39**.

42. Menter, F.R., *Zonal Two Equation k-ω Turbulence Models for Aerodynamic Flows.* 24th Fluid Dynamics Conference, 1993.

43. Thompson, S., *Effect of Cooling Rate on Solidification Characteristics of Aluminum Alloys A356 and AA5182.* 2003.

44. B. Freeze, S.S., N. Morley, M. Abdou, *Characterization of the effect of Froude number on surface waves and heat transfer in inclined turbulent open channel water flows.* International Journal of Heat and Mass Transfer, 2003: p. 3765-3775.

45. FishXing. *Froude Number and Flow States*.

46. Hsueh-Chia Chang, E.A.D., *Complex Wave Dynamics on Thin Films.* 2002.

47. Panton, R.L., *Incompressible flow* 2006.

48. Corfield, F.M.W.a.I., *Viscous fluid flow*. 2006: McGraw-Hill Higher Educatio Boston.

49. Hermann Schlichting, K.G., Egon Krause, Herbert Oertel, *Boundary-layer theory*. Vol. 7. 1955: Springer.

50. Heidelberg-Lecture, I., *Fluid Instabilities*